This is a repository copy of *New rosette tools for developing rotational vibration-assisted incremental sheet forming*.

White Rose Research Online URL for this paper:
https://eprints.whiterose.ac.uk/209029/

Version: Published Version

New rosette tools for developing rotational vibration-assisted incremental sheet forming

H. Long *, W.X. Peng , Z.D. Chang , H. Zhu , Y.J. Jiang , Z.H. Li

Department of Mechanical Engineering, the University of Sheffield, Sheffield, UK

ABSTRACT

A major limitation of the incremental sheet forming (ISF) is its difficulties to manufacture hard-to-form materials. The existing ISF process variants require additional systems or devices, which compromises the process flexibility and simplicity, the unique advantages of the ISF. In this study, a novel type of rosette tools is proposed for developing a new ISF process to improve material formability, named as Rotational Vibration-assisted ISF (RV-ISF). A hard-to-form material, magnesium alloy AZ31B, has been successfully formed in the RV-ISF experiment by creating low-frequency and low-amplitude vibrations, and elevated temperatures at the local forming zone in the range of 250–450 °C. By developing the new RV-ISF, it has achieved a 60% increase in fracture depth than that by friction-stir ISF and more than 46% reduction in forming force than that by the conventional ISF. Experimental evaluation and analytical prediction of temperature increase, forming force and flow-stress reduction have concluded that the combined thermal effect and vibration softening is the key mechanism leading to the significant formability enhancement. The results show that both the rosette tool design and tool rotational speed are critical factors determining heat generation and transfer as well as vibration frequency and amplitude. Investigation on microstructural evolution has revealed that the low-frequency and low-amplitude vibrations created by the rosette tool have activated dislocations and dynamic recrystallization, and produced refined grains and increased micro hardness. The new RV-ISF developed has potentials to manufacture other hard-to-form materials and complex geometries of sheet products, overcoming the formability limitation of the current ISF technology.

1. Introduction

Incremental sheet forming (ISF) attracted considerable attention due to the flexibility offered by the process in manufacturing small-batch and customised sheet products. Emmens et al. (2010) conducted a review on the historical development of ISF. In an environmental focused study, Cooper and Gutowski (2020) predicted significant energy and cost savings for the US car industry through implementation of ISF. ISF has a number of variants including single-point and two-point incremental forming (SPIF and TPIF) and double-sided incremental forming (DSIF). Duflou et al. (2018) presented a comprehensive review of the state-of-the-art and future prospects of SPIF and highlighted the potential of the ISF for a large number of application domains. Although many unique advantages were identified, Attanasio et al. (2008) and Hirt et al. (2021) reported that industrial adoption of the ISF technology was still limited due to low geometrical accuracy, rough surface finishing, and fracture caused by sheet thinning during ISF processing. Another critical

limitation of the ISF is its difficulties to manufacture hard-to-form materials because of their poor ductility when processed at room temperature. To overcome the formability limitation of the ISF, heat-assisted and vibration-assisted ISF processes were investigated.

Ambrogio et al. (2008) designed a heater band and insulation chamber in SPIF to form magnesium alloy AZ31 at targeted temperatures of 200–300 °C that improved the formability of the material. Duflou et al. (2007) proposed a laser-assisted ISF process by localised heating of the deforming sheet that reduced forming forces, improved dimensional accuracy and increased formability for a range of materials. Fan et al. (2008) proposed an electric hot ISF (E-ISF) by making use of electric current passing through the deforming sheet that successfully formed magnesium alloy AZ31 and titanium alloy TiAl2Mn1.5. Xu et al. (2016) developed an electrical-assisted double-sided ISF (E-DSIF) and designed a force control device to ensure a stable tool-sheet contact. However, surface quality and geometrical distortion of the formed parts are the two major issues due to the extremely high temperature at local

areas in the electrically assisted ISF processes. Otsu et al. (2010) proposed the friction stir-assisted ISF (FS-ISF) in which a hemispherical tool was rotated under a high speed, ranging from 1000 to 10,000 rpm to form magnesium alloy. Otsu et al. (2011, 2014) further studied forming aluminium alloys. To reduce friction at the tool-sheet interface and control the level of heat generation in the FS-ISF, Xu et al. (2013) developed a forming tool with laser etched surface texture. Xu et al. (2014) conducted a follow-on comparative study in forming magnesium alloy AZ31B by the FS-ISF and E-ISF and concluded a higher processing efficiency of the FS-ISF. To reduce the undesirable frictional effect on surface quality, Lu et al. (2014) developed an oblique roller-ball tool that showed an improved surface quality than that using the hemispherical tool. To overcome the contradicting effect of process variables on formability and surface quality in the FS-ISF, Wang et al. (2020) proposed a processing window in the FS-ISF of AA2024 for generating higher forming temperatures while achieving a reasonable surface quality.

Ultrasonic vibration assisted ISF (US-ISF) processes have been explored by a few recent studies. Vahdati et al. (2017) and Amini et al. (2017) applied ultrasonic vibration to the tool in forming straight grooves in the SPIF experiment of AA 1050-O sheets, under vibration frequency of 20 kHz and vibration amplitude of 7.5 μm. Amini et al. (2017) found that the vertical forming force was decreased by up to 36% and the formability was enhanced by up to 48%. Yang et al. (2019) applied a varied range of vibration frequency and amplitude in US-SPIF of AA1060 sheets and found that the formability was improved under vibration frequency of 25 kHz and vibration amplitude of 6 μm. However, higher vibration frequencies and amplitudes caused sheet cracking because of greater plastic strains in the direction of the ultrasonic vibration being applied. Effects of process parameters in US-ISF processes were also investigated, including tool diameter, feed rate, and vibration amplitude by Long et al. (2018). as well as tool rotational speed by Amini et al. (2018). Long et al. (2018) found that significant forming force reductions and temperature increases could be achieved under conditions of higher ultrasonic energy input and lower tool feeding speed. Amini et al. (2018) concluded that combining tool rotation with tool ultrasonic vibration significantly reduced surface roughness. By employing both experiment and finite element (FE) modelling, Li et al. (2017a) investigated forming force variations during the US-SPIF of Q235 steel under various vibration frequencies and amplitudes. It was found that the vertical forming force decreased significantly when applying vibration frequency up to 40 kHz and amplitude up to 40 μm. However, if the frequency and amplitude applied were beyond these levels, the vertical forming increased significantly. Cheng et al. (2019) applied the longitudinal ultrasonic vibration to a hemispherical tool at 20 kHz oscillating frequency in both SPIF and TPIF processes and observed a significant tool force reduction in the US-TPIF process. By developing a constitutive model under ultra-high strain rates, Zhang et al. (2021) investigated the effects of tool size, rotational speed, feed rate, tool pitch, and vibration amplitude on the reduction of forming force and springback of material AA1050 in US-ISF. Li et al. (2017b) investigated effects of different vibration amplitudes at 5, 10 and 20 μm under vibration frequency of 20 kHz in US-SPIF of two aluminium alloys AA1050 and AA5052. It was found that the forming force was reduced considerably with an increasing vibration amplitude especially at later stages of ISF process, and the ultrasonic softening effect was more obvious for the material with higher yield strength. In a follow-on study, Cheng et al. (2022) developed a hybrid constitutive model for AA1050-O in a FE simulation of the US-SPIF and the microstructure characterisation results showed the occurrence of relative larger grains and an increase of low angle grain boundaries (LAGBs) indicating the occurrence of ultrasonic-activated dynamic recovery of the material. By developing a physics-based constitutive model, and conducting experiment and FE modelling in ultrasonic vibration assisted forming by using vibration amplitudes from 5 to 20 μm, Sedaghat et al. (2019) suggested that greater vibration amplitudes led to an increased reduction in material flow stress. However, in these US-ISF studies, only low strength aluminium alloys of AA1050 and AA5052 and steel Q235 have been investigated. The potential of applying ultrasonic vibration in ISF to improve the formability of hard-to-form materials is yet to be demonstrated.

Mechanical vibration assisted ISF processes have also been explored in few studies. Lu et al. (2017) developed an elliptical tool to enable tool rotation-induced vibration in ISF (V-ISF) of magnesium alloy AZ31B. Wu et al. (2022) adopted the same idea of the elliptical tool design by Lu et al. (2017) but used a hemispherical tool with flat head and compared the results of the V-ISF and FS-ISF in forming a hyperbolic cone of AA5052-H32. Xiao et al. (2022) developed a forming tool-connecting device consisting of a motor and cam system to provide the tool with longitudinal low-frequency vibrations from 0 to 100 Hz and amplitude from 0 to 100 μm in SPIF of AA1050 sheets. Nasulea and Oancea (2021) developed a circumferential hammering tool to reduce geometrical inaccuracies of SPIF formed parts without the necessity of implementing other complex solutions. Compared to the US-ISF processes employing vibrations with high frequencies and low amplitudes, the tool rotation in the V-ISF generated relatively low vibration frequencies but higher vibration amplitudes. Laminated ultrafine grains and higher micro hardness have been observed at the inner side of the formed hyperbolic cone by Lu et al. (2017); however further study and microstructure characterisation are necessary to understand the mechanism of formability enhancement in V-ISF.

Vibration effects on material plastic deformation behaviour have been investigated by a few studies. Zhou et al. (2018) conducted ultrasonic vibration assisted compression experiments of aluminium and titanium alloys, demonstrating that the ultrasonic softening effect on the flow-stress reduction was not only influenced by vibration amplitude but also by the vibration frequency. Although the ultrasonic softening effect was enhanced by increasing the vibration amplitude, increasing vibration frequency above a certain limit had reduced the ultrasonic softening effect, reported by Zhou et al. (2018). Blaha and Langenecker (1959) and Langenecker (1961, 1966) concluded that the preferential absorption of acoustic energy by lattice imperfections activated dislocations and reduced the resolved shear stress required for substantial dislocation migration on the slip plane, resulting in softening. Pohlman and Lehfeldt (1966) performed both ultrasonic oscillation assisted wire drawing and bending experiments that showed reductions of friction and forming forces being proportional to the amplitude of ultrasonic oscillation. Their findings also provided explanations that the flow-stress reduction in the ultrasonic vibration assisted processes, in addition to the activation of dislocations, was due to the superimposition of the alternating acoustic stress on the stress produced externally. Green (1975) discussed the interaction between ultrasonic waves and dislocations that had resulted in work softening and stress reduction by increasing the amount of plastic strain; however, the interaction also resulted in work hardening by causing the dislocations to become less mobile. Huang et al. (2009) found that the magnitude of acoustic softening effect was linearly proportional to the ultrasonic vibration amplitude and concluded that the characteristics of the atomic structure, such as the condition of the lattice structure and the number of imperfections, might have a greater effect on the acoustic softening than the material properties themselves. Siu et al. (2011) conducted indentation experiments simultaneously excited by ultrasound and concluded that the softening effect by the latter constituted recovery associated with extensive enhancement of subgrain formation during deformation. The enhanced subgrain formation was resulted from the combined application of the quasi-static loading and the ultrasound. Yao et al. (2012) developed a crystal plasticity model to investigate the acoustic softening and acoustic residual hardening by applying the thermal activation theory and dislocation evolution theory. Their results showed that the stress reduction due to the acoustic softening was proportional to the vibration amplitude, while the acoustic residual hardening effect was influenced by both the vibration amplitude and duration. In addition to

the ultrasonic softening effect, Yao et al. (2012) and Zhou et al. (2018) also found that the ultrasonic vibration could lead to the residual hardening effect to aluminium alloys but residual softening effect to titanium alloys. Lum et al. (2009) explained that the ultrasonic vibration could induce sufficient heating to cause the annealing effect and reduce the dislocation, leading to residual softening effect. Zhou et al. (2017) conducted a comparative study of two different materials undergoing ultrasonic assisted compression, the microstructural characterisation by Electron Backscatter Diffraction (EBSD) revealed that for aluminium, the ultrasonic vibration reduced the grain size and changed the orientation of the grain boundaries, both contributed to the residual hardening effect. On the other hand, for titanium alloys, the grain refinement induced by ultrasonic vibration was limited; the ultrasonic vibration could promote saturation of twinning and reduced fraction of twinning boundaries, contributing to the residual softening effect. However, these studies could not explain the material deformation behaviour under vibration assisted ISF with cyclic plastic deformation and superimposed tool vibration on the quasi-static forming loading.

It is clear that the FS-ISF has maintained the process simplicity and flexibility without the need of employing additional devices for providing localised heating. However, as the interfacial friction is the only heat generation mechanism to improve the formability by forming at elevated temperatures, the adverse effects of friction on poor surface quality, uncontrollable forming temperature, and severe tool wear are major limitations of the FS-ISF, as reported by Xu et al. (2016, 2013, 2014), Lu et al. (2014) and Wang et al. (2020). The ISF processes assisted by ultrasonic or mechanical vibrations have shown great potentials on the formability enhancement but investigations on hard-to-form materials are limited. The combined thermal effect and vibration softening on formability improvement in ISF is unclear. Furthermore, the mechanisms of vibration softening on flow-stress reduction by dislocation activation and dynamic-static stress superimposition under low-frequency vibrations in ISF have yet to be investigated.

In order to develop an ISF process not only maintaining its process simplicity and flexibility but also being capable of forming hard-to-form materials and complex geometries, this study develops a new rotational vibration-assisted ISF (RV-ISF) process by employing a novel type of rosette tool design to improve the material formability. By examining the capability of the new RV-ISF process, the mechanisms of the combined thermal effect and vibration softening leading to the formability improvement are investigated. Vibration frequencies and amplitudes in the RV-ISF process are characterised by conducting the contact analysis of the rosette tool, FE vibration modelling and experiment. RV-ISF experimental tests of magnesium alloy AZ31B are performed to demonstrate a significant improvement in formability of a hard-to-form material and to evaluate the correlation of forming force reduction with the combined thermal and vibration effect. Effects of key process parameters, including tool design, tool rotational speed, and material deformation modes, on sheet fracture strain are investigated. Thermal modelling of heat generation and heat transfer is developed to evaluate the effect of interfacial friction and plastic deformation on temperature increase in the RV-ISF. Analytical modelling of the tool rotation induced vibration softening in the RV-ISF is also developed to evaluate flow-stress reduction due to stress superimposition and vibration energy activated dislocations. By performing EBSD scanning of the RV-ISF formed samples, the microstructure evolution is analysed to evaluate vibration-activated dislocations during RV-ISF. The findings from the experiments, modelling and analysis lead to new understanding of the combined thermal effect and vibration softening on the significant formability enhancement in the RV-ISF.

2. Analysis of tool rotation induced vibration in the RV-ISF process

2.1. Contact analysis of the rosette tool

In a conventional SPIF process, it only requires a simple hemispherical tool to deform a sheet material locally and incrementally by moving the tool along a predefined tool path created directly from the CAD model of a desired geometry. In this study, a new type of the rosette tool with a number of grooves is developed. By rotating the tool, it generates vibrations of the deforming sheet at tool-sheet contact. Fig. 1a, b show illustrations of the RV-ISF and periodic surface contacts between the tool head and inclined wall of the deforming sheet. During the tool rotation, grooves on the tool head create localised cyclic vibrations of the deforming sheet, as shown in Fig. 1c. Different from all existing vibration assisted ISF processes, in the RV-ISF, the tool rotation induced vibration of the deforming sheet is dependent on a specific tool geometry, tool rotational speed and the wall angle of a part formed.

To evaluate the rosette tool design on vibration characteristics of the deforming sheet, the variation of the contact area between rosette tool and sheet due to grooves on the tool surface is evaluated. Fig. 2a illustrates that a sheet blank is plastically deformed under the tool feed motion. Using a rosette tool of four-grooves, 90° pitch, the tool design parameters considered are the tool radius r, and groove depth D and width W. By assuming the tool-sheet contact area, A_1, can be considered as an elliptical shape, as reported by Chang et al. (2019), it can be shown

$$A_1 = \frac{\pi r}{2}\left(h_1 + r(1-\cos\alpha)\frac{l_1}{l_2}\right)$$

$$= \frac{\pi r}{2}h_1 + \frac{\pi r^2(1-\cos\alpha)\arccos\left(\frac{W}{2r}\right)}{2\alpha} \quad where \ \ h_1 = \sqrt{\frac{2ht}{r}} \tag{1}$$

where $t = t_0 \cos\alpha$ is the deformed sheet thickness, t_0 is the initial sheet thickness, α is the wall angle, and h is the step size of the tool path. By cutting a groove on the hemispherical tool surface, the area of the intersection between groove and contact area, A_2, can be expressed as

$$A_2 = A_2'\left(\frac{l_2 + D - \frac{\pi r}{2}}{D^2}\right)^2 = \frac{2rD}{\pi}\arcsin\frac{W}{2r}\left(1 + \frac{r\alpha}{D} - \frac{\pi r}{2D}\right)^2 \ where$$

$$A_2' = \frac{2rD}{\pi}\arcsin\frac{W}{2r} \tag{2}$$

where A_2' is the groove area. The reduction of the contact area A_1 due to cutting a groove on the tool surface can be evaluated by the ratio of the two areas, A_2/A_1. Fig. 2b shows the effect of the wall angle and groove dimensions on the reduction of the contact area due to cutting grooves on the tool surface. A greater wall angle increases the ratio thus a higher reduction of the contact area, producing a greater vibration effect and a reduced frictional heating due to periodic loss of contacts. By increasing either groove length or width it increases the reduction ratio of the contact area proportionally thus creating a greater vibration effect of the deforming sheet. Increasing the tool radius reduces the ratio; the step size shows a relative small effect on the contact area reduction. Following on the contact analysis, the rosette tools with three grooves (T3) and four grooves (T4) are developed to evaluate the effect of a varied degree of frequency, as shown in Fig. 3. To compare the effect of tool rotation in the RV-ISF with that in FS-ISF and V-ISF, the hemispherical tool (T0) and the elliptical tool with double offsets (T2), shown in Fig. 3, are also tested.

2.2. Vibration measurement and FE modelling

To measure local vibration frequencies and amplitudes of the deforming sheet, RV-ISF experimental tests are conducted and an Eddy
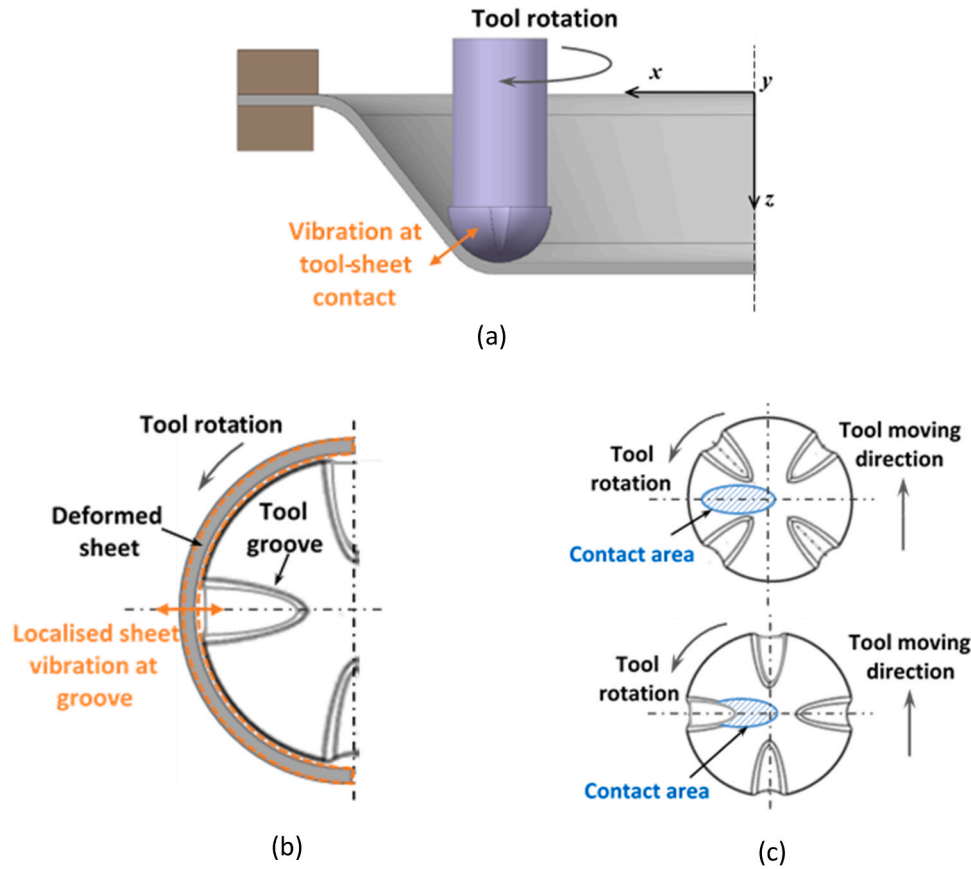
Fig. 1. Illustration of periodic tool-sheet contact and localised sheet vibration in the RV-ISF. (a) Rotational vibration assisted ISF (RV-ISF); (b) Localised sheet vibration at groove of the rosette tool; (c) Rosette tool-sheet contact areas, away from groove and at groove of the tool.

current sensor (CSH1-CAm1 from MICRO-EPSILON) is used for measurements. The Eddy current sensor is positioned at a fixed distance of 1 mm to the wall of a formed pyramid with a wall angle of 50° at the forming depth of 30–40 mm, as shown in Fig. 4a. Tool T2 and T4 used in the experiment are shown in Fig. 4b. In the tests of vibration measurements, the tool rotates under a constant speed of 2000 and 3000 rpm respectively and tool feed rate is 1000 mm/min. The sheet displacement data is recorded when the tool moves past the sensor position. The data is processed through centralisation and discrete Fourier's transformation to calculate the vibration frequencies and amplitudes of the deforming sheet.
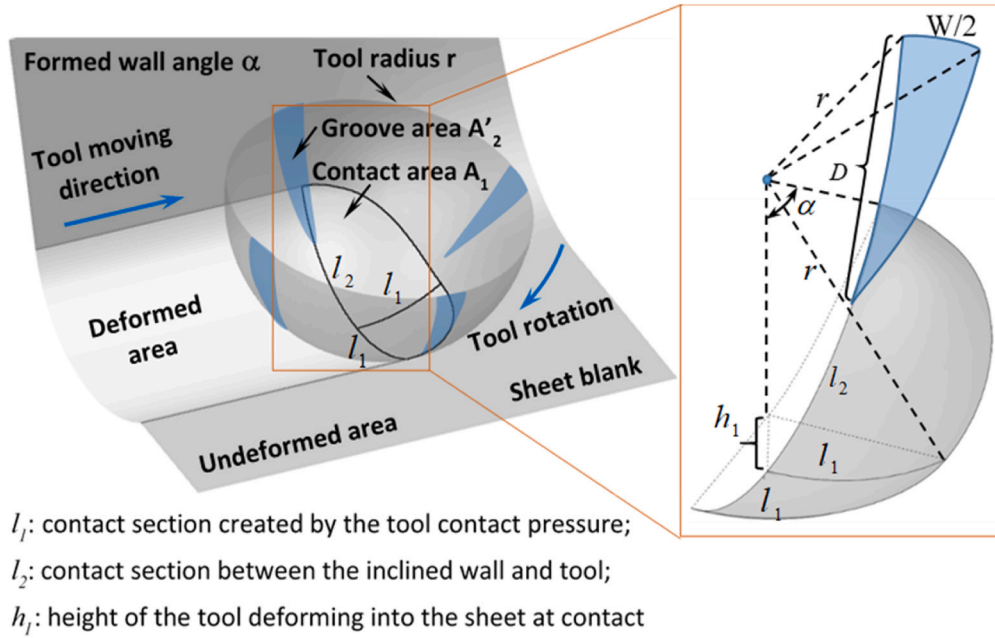
For better understanding of the measured frequencies and amplitudes in the RV-ISF, FE vibration modelling of the deforming sheet in the RV-ISF is also developed under the same condition of the experimental tests by using FE software ABAQUS. For simplification, the FE model of using each tool design consists of a pre-formed sheet at a forming depth of 30 mm, as shown in Fig. 5. The forming tool moves down for a step size of 0.5 mm and continues to follow the designed circular toolpath on a fixed forming layer. Material plasticity is defined by applying the Johnson-Cook (J-C) model, as shown in Eq. (3). The J-C model parameters and material properties required in the FE models are given in Table 1. For FE meshing, 8-node brick element type with reduced integration (C3D8R) is used for the deforming sheet while 4-node tetrahedral element type (C3D4) is used for the forming tool, and the meshed elements have a global size of 1 mm. A stable time increment is defined at 1.12×10^{-5} seconds. The field output is requested at every 0.001 s, so that the sampling frequency of the sheet displacement change comes as 1000 Hz. The processing method for determining frequencies and amplitudes is the same as that used for the experimental results by extracting the displacement-time data of a selected node at the upper boundary of the contact area.

$$\sigma = (A + B\varepsilon^n) \left[1 + C\ln\left(\frac{\dot{\varepsilon}}{\dot{\varepsilon}_{ref}}\right) \right] \left[1 - \left(\frac{T - T_{ref}}{T_{melt} - T_{ref}}\right)^m \right] \tag{3}$$
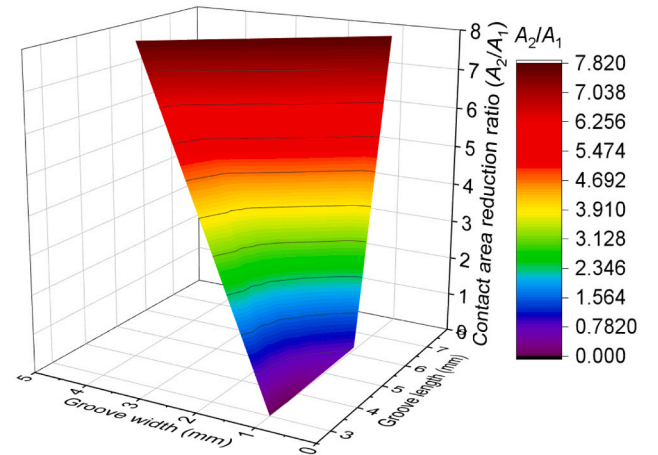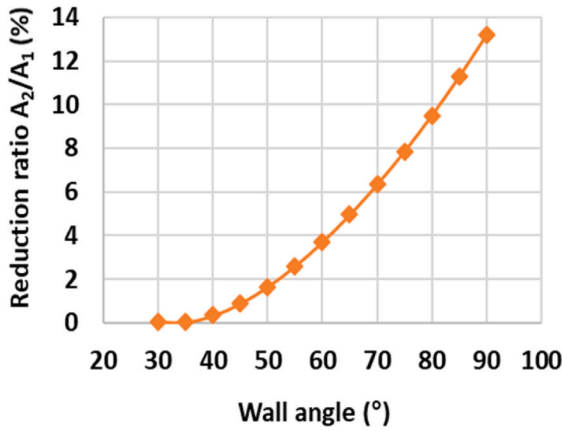
2.3. Characterisation of vibration frequencies and amplitudes

Vibration frequencies and amplitudes obtained from the experimental measurement and FE modelling by using tools T2 and T4 under two different rotational speeds are shown in Fig. 6 and summarised in Table 2. From the results of the RV-ISF measurement and FE modelling by T2 and T4, fundamental frequencies are found to be the same as the reference frequency, as calculated in Table 2. As can be seen in Fig. 6, at a higher frequency range, second and even third harmonics can be observed, usually occurring at integer multiples of the reference frequency. At the lower frequency range of the experimental results, the smaller peaks show subharmonics but no obvious subharmonics are observed in the FE modelled results. Further FE modelling results show these low frequencies are not the natural frequencies of the deformed sheet. It is considered that these may be resulted from the tool system runout and tool surface wear, as well as machine system related effects. Specifically, using tool T2, the measured vibration frequencies match closely with the FE modelled values, however, the measured vibration amplitudes are approximately twice of the FE modelled values under low frequencies but correlated better under higher frequencies, as shown in Fig. 6a and Table 2. The reason for the underestimated amplitude under low frequencies by the FE models may be the delayed sheet response to material elastic recovery in the FE modelling. For tool T4, both the measured frequencies and amplitudes are similar to the FE modelled values, as shown in Fig. 6b and Table 2.

The vibration results using tools T2 and T4 confirm that the RV-ISF process has much lower vibration frequencies, in the range of

l_i: contact section created by the tool contact pressure;

l_2: contact section between the inclined wall and tool;

h_i: height of the tool deforming into the sheet at contact

(a)

(b)

Fig. 2. Contact analysis of the rosette tool. (a) Sheet deformation caused by tool feed motion and the definition of contact area and groove area; (b) Parametric evaluation of the rosette tool design on the ratio of contact area reduction ($t_0 = 1$ mm, $\alpha = 30$–$90°$, $r = 3$–7 mm, $D = 2$–7.5 mm, $W = 0.5$–4.5 mm, $h = 0.1$–1 mm).

67–400 Hz if tool rotational speed is 2000–6000 rpm, in comparison with the ultrasonic vibration assisted ISF process, typically operating in the range of 20 kHz frequency. The double offset tool with offsets 2×1 mm, T2, creates significantly higher vibration amplitudes than that produced by the four-groove rosette tool T4 with groove depth of 6 mm and groove width of 2.5 mm. Under a tool rotational speed of 2000 to 3000 rpm, for T4, the amplitudes measured by the experiment vary from 2–11 μm, much smaller than 18–80 μm generated by T2. When using the same tool, the amplitudes show a reducing trend with an increasing tool rotational speed. The reason may be that within one vibration cycle when the tool contacts the deforming sheet, if the rotational speed is higher than a certain limit, there is insufficient time for the elastic deformation of the sheet to be recovered, resulting in a reduced vibration amplitude.

3. RV-ISF formability experimental method and results

3.1. Fracture depth and fracture strain

RV-ISF experimental tests for formability evaluation are carried out on a 3-axis CNC machine (SIEMENS XYZ 1060HS VMC). To record the tool forming force time history during the RV-ISF, a 3-component piezoelectric force transducer (Kistler 9367 C) is placed under the sheet fixture. An infrared thermal camera (FLIR T650sc) is used to record the sheet temperature variation, positioned approximately at a 40° inclined angle between camera lens and workbench of the CNC machine. A hard-to-form material, magnesium alloy AZ31B, is selected to investigate if the RV-ISF process can improve the formability. In the experiment, rosette tools of three-grooves, T3, and four-grooves, T4, with groove depth of 6 mm and groove width of 2.5 mm are tested and compared with four-grooves T4R with reduced groove depth of 4 mm and groove width of 2 mm. Two forming geometries, a truncated
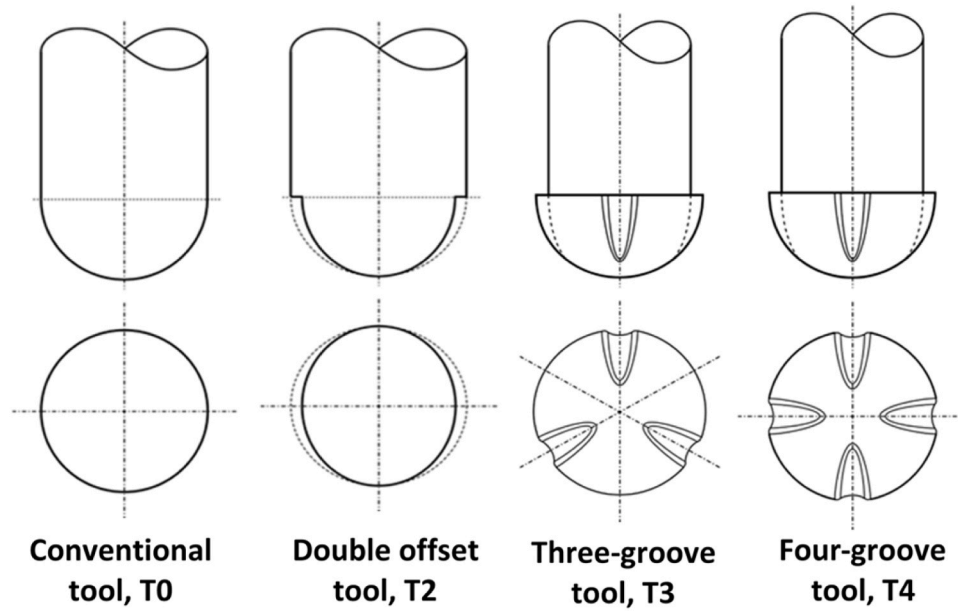
Fig. 3. Tools tested: hemispherical tool (T0), double offset tool (T2) with offsets = 2 × 1 mm, rosette tools of 3-groove (T3) and 4-groove (T4) with groove depth = 6 mm and groove width = 2.5 mm, using a radius of 5 mm for all tools.
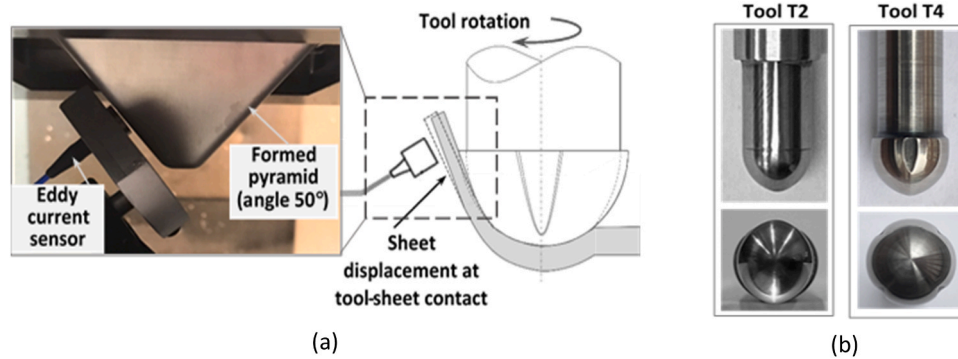

Fig. 4. Measurement of sheet vibration frequencies and amplitudes. (a) Position of Eddy current sensor; (b) Double offset tool T2 with offsets = 2 × 1 mm and 4-groove rosette tool T4 with groove depth = 6 mm and groove width = 2.5 mm.

hyperbolic cone and pyramid are designed because they have an increasing wall angle with increasing forming depth thus an increasing difficulty to deform the sheet without fracture. When forming the hyperbolic cone and pyramid geometries, the material experiences different deformation modes; the hyperbolic cone is under plane strain while for the hyperbolic pyramid the deformation varies between plane strain and biaxial stretching. By testing two different geometries, the effect of the tool designs on the material deformation modes can be investigated.

Fig. 7a shows examples of the hyperbolic cone formed by using AZ31B sheets. Fig. 7b,c show fracture depth and fracture strain results from the tests using tools T0, T2 and T4 under different tool rotational speeds, step sizes of 0.3 and 0.5 mm, and sheet thicknesses of 1 mm and 1.6 mm, respectively. For the tools tested, higher tool rotational speeds significantly increase the fracture depth and fracture strain; however, after reaching a certain speed limit, depending on the tool design, the fracture depth starts to decrease. For the rosette tools tested, the rotational speed range of 3000–6000 rpm has achieved an improved fracture depth and fracture strain. Thicker sheets achieve the highest fracture depth and fracture strain even under lower tool rotational speeds. A smaller step size of the tool path slightly improves the fracture depth but it shows a greater effect when tool T2 is used.

Without tool rotations, the sheet is fractured soon after the test starts, with a very small fracture depth of 5.4 mm. By comparing the RV-ISF using T4 with the FS-ISF using T0 under rotational speed of 3000 rpm, the fracture depth of 35.7 mm in the RV-ISF shows a 60% increase than the fracture depth of 22.3 mm in the FS-ISF when forming 1.6 mm thickness sheets, as shown in Fig. 7b. Tool T4 achieves greater fracture depths and fracture strains than tool T2, as shown in Fig. 7b,c. T4 is able to achieve higher fracture strains under lower rotational speeds than that by T2, indicating each tool has its own optimised rotational speed range. Considering T4 has much lower amplitudes than that of T2, these results indicate that if the amplitudes created by a tool are too high, such as that of T2, the fracture strain reduces. The difference in fracture depth and strain results by using T2 and T4 also show that both vibration amplitude and frequency are important for formability improvement.

To investigate the effect of material deformation modes on formability in the RV-ISF, the hyperbolic pyramid is formed by using AZ31B sheets of 1 mm thickness. The rosette tools with three-grooves T3 and four-grooves of reduced grooved dimensions T4R, as shown in Fig. 8c, are tested. Fig. 8a,b show examples of the hyperbolic pyramid formed and the fracture depth obtained under different tool rotational speeds. Fig. 8b shows all pyramid tests produce higher fracture depths than that of the hyperbolic cone tests. This may be explained by the difference in
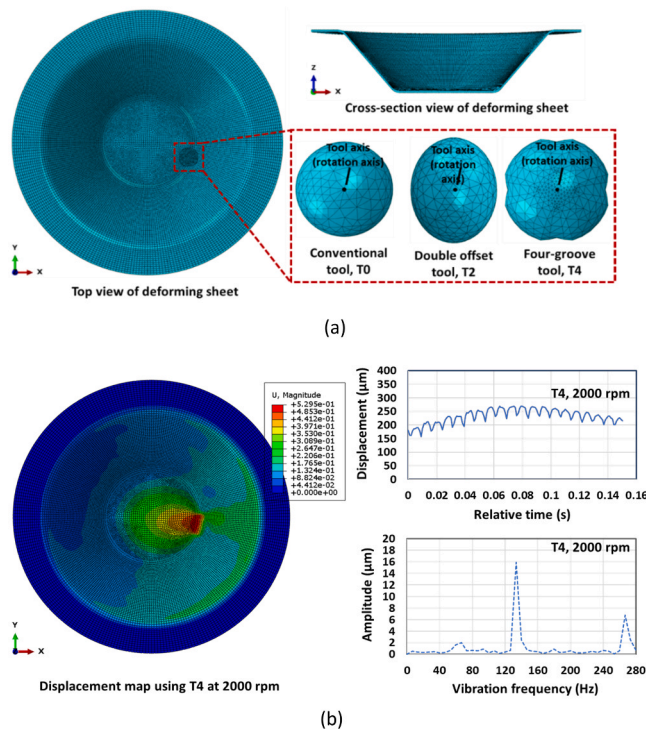
(a)

(b)

Fig. 5. FE simulation of tool rotation induced sheet vibration in the RV-ISF. (a) FE models using tool T0, T2, and T4; (b) Modelled sheet displacement and vibration frequencies and amplitudes at tool-sheet contact.

sheet deformation modes between two geometries. The deformation mode when forming a hyperbolic cone can be considered as plane strain. In forming a hyperbolic pyramid, the deformation mode of the sheet varies between plane strain and biaxial stretching, occurring at each corner of the pyramid, which may cause the sheet fracture at these locations if employing the conventional ISF. However, by employing the rosette tools, both vibration effect and frictional heating effect are enhanced at the corners of the pyramid due to an increased contact area between tool and deforming sheet that delays the sheet fracture. This indicates that the RV-ISF process is capable of achieving higher form-ability under multiaxial stress conditions. By comparing the fracture depth obtained by using T4 and T4R, it shows that the tool T4R with smaller groove dimensions operated under lower rotational speeds also achieves excellent results of the fracture depth.

3.2. Correlation of force reduction with vibration and temperature

Fig. 9 shows the measured vertical tool force when forming the hyperbolic cone using AZ31B sheet of thickness of 1 mm by T2 and T4 under tool rotational speed of 7000 and 6000 rpm, respectively. The selection of the different speeds for comparing the tool force results is because they are the rotational speeds when T2 and T4 have achieved their highest fracture depth respectively, as shown in Fig. 7b, as the analysis is to evaluate the formability improvement. The tool force using

T0 without tool rotation is also presented as a reference. At the initial forming stage, there is no obvious difference in the force-time histories between tools T0 and T4 by creating low vibration amplitudes. This is because when forming a small wall angle of the cone at an early stage of the process, the tool rotation induced vibration has not taken its effect of impact on the sheet surface, as shown in Fig. 9a. As the process progresses, comparing time I, II and III as shown in Fig. 9a,b, an increasing effect of the tool-induced vibration results in greater cyclic variations of the vertical force when the wall angle becomes greater with increasing forming depth, which resulting in an increased contact area between tool and sheet. Due to the different vibration amplitudes created by T2 and T4, it is clear that the vibration amplitude directly affects the variations of the vertical tool force. By comparing the maximum vertical force using T0 and T4, the vertical force by using the rosette tool T4 in RV-ISF is reduced to 46% of that in the SPIF by using T0.

Fig. 10 shows the measured vertical force and local sheet temperature together when forming the hyperbolic cone using AZ31B sheet of thickness 1 mm by tool T4 under rotational speed of 6000 rpm. As can be seen in Fig. 10a, the vertical force increases sharply at the initial forming stage and reaches a maximum value of just below 400 N but displays a sudden drop when the average temperature reaches 200 °C. While the temperature continues to increase from 200 to 300 °C, the forming force remains nearly unchanged which may be explained by a balanced state due to strain hardening under increasing wall angle at greater forming depth. The subsequent stage is a gradual reduction of the forming force when the average temperature keeps an increasing trend towards the end of the process, reaching a maximum value of 450 °C. The tool force reduction is closely correlated with the increase of local sheet temperature as the material AZ31B is softened significantly at the temperature range of 200–350 °C. As shown in Fig. 10b, when the tool moves along its tool path, the local temperature of the sheet changes cyclically, the temperature is the highest at the tool-sheet contact (zone A) and it reduces while the tool moves away from the contact (zone B).

To compare the RV-ISF with the FS-ISF, Fig. 11 shows variations of the measured vertical tool force and local sheet temperature from the FS-ISF process when forming a hyperbolic cone using AZ31B sheet of thickness 1.6 mm by tool T0, under rotational speed of 4000 rpm. Unlike that observed in the RV-ISF, the vertical force continues a sharp increase trend after the initial stage of the process, reaching the maximum force of 720 N at time 260 s. As can be observed, the sheet temperature only has significant increases after time 260 s, which results in a sharp reduction of the vertical force after time 300 s. A considerable large range of temperature variations can be seen and the sheet temperature reaches a maximum temperature over 500 °C. Afterward, the vertical force shows a steady reduction trend. The considerable temperature variations can be explained by the contact condition of tool T0, which is in full contact with the sheet during the entire duration of the process. It is difficult to control frictional heating to achieve a uniform sheet temperature that is desirable to improve the formability. These observations are in agreement with the reported limitations of the FS-ISF by Xu et al (Xu et al., 2016, 2013, 2014). and Lu et al (Lu et al., 2014). It is clear that the elevated sheet temperature is directly correlated with the dramatic reduction of the vertical forming force after time 300 s. Comparing the two processes, in the RV-ISF, the temperature variation is relatively uniform, maintaining an increasing

Table 1

J-C model parameters and material properties of AA5052 used in FE vibration modelling.

J-C yield strength A (MPa)	J-C hardening coefficient B (MPa)	J-C strain hardening exponent, n	J-C softening exponent, m	Melting temperature T_{melt} (K)	Reference temperature T_{ref} (K)
170	325.4	0.5119	0.8577	893	298

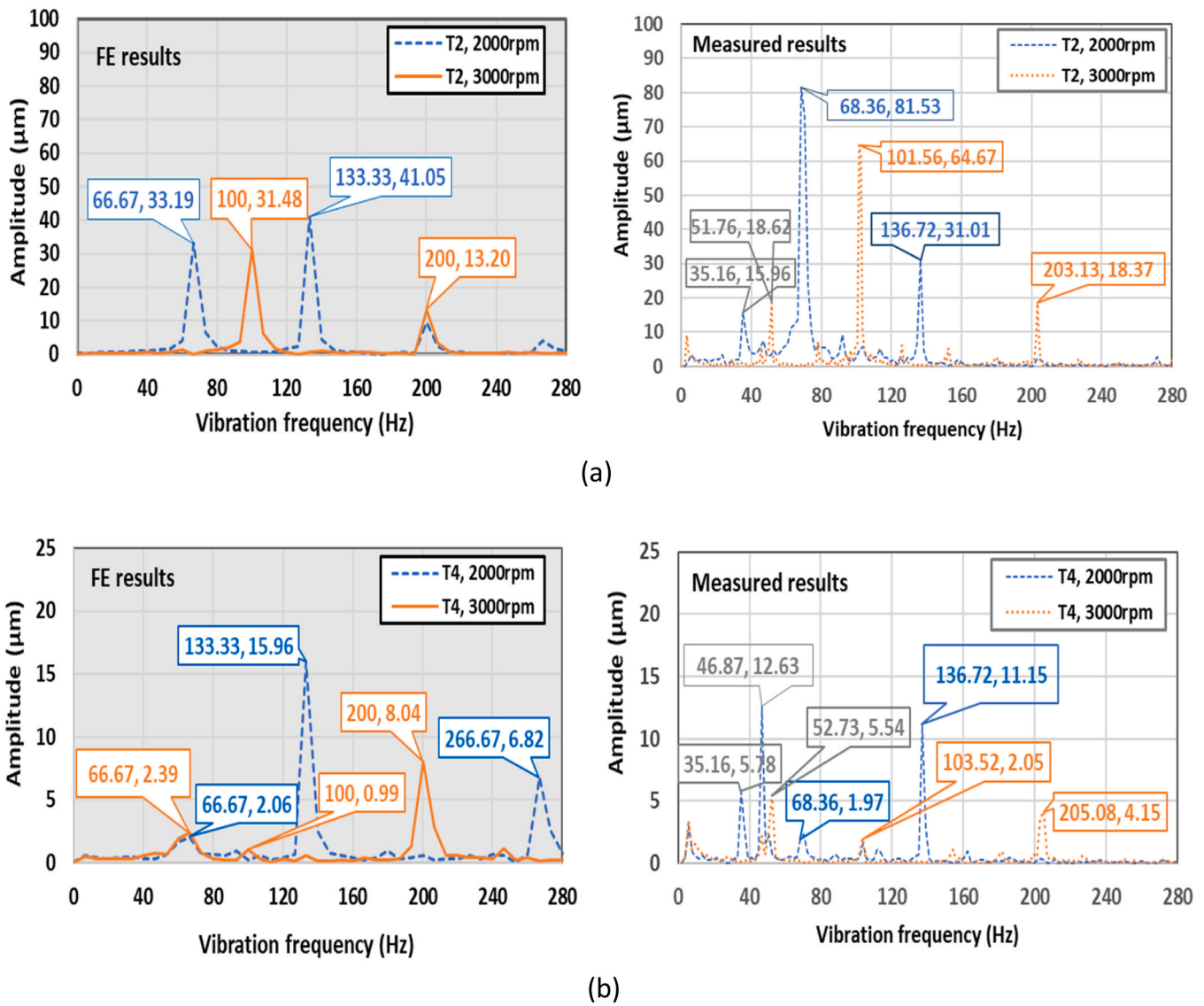| J-C strain rate constant, C	Reference strain rate $\dot{\varepsilon}_{ref}$ (s^{-1})	Density (kg/m^3)	Young's modulus (MPa)	Poisson's ratio	Coefficient of friction
0.02	0.1	2680	69300	0.33	0.05

Fig. 6. Comparison of FE modelled and experimental measured vibration frequencies and amplitudes in the RV-ISF. (a) T2 and (b) T4, under rotational speed of 2000 and 3000 rpm.

Table 2
Characterisation of frequencies and amplitudes of sheet vibration in RV-ISF.

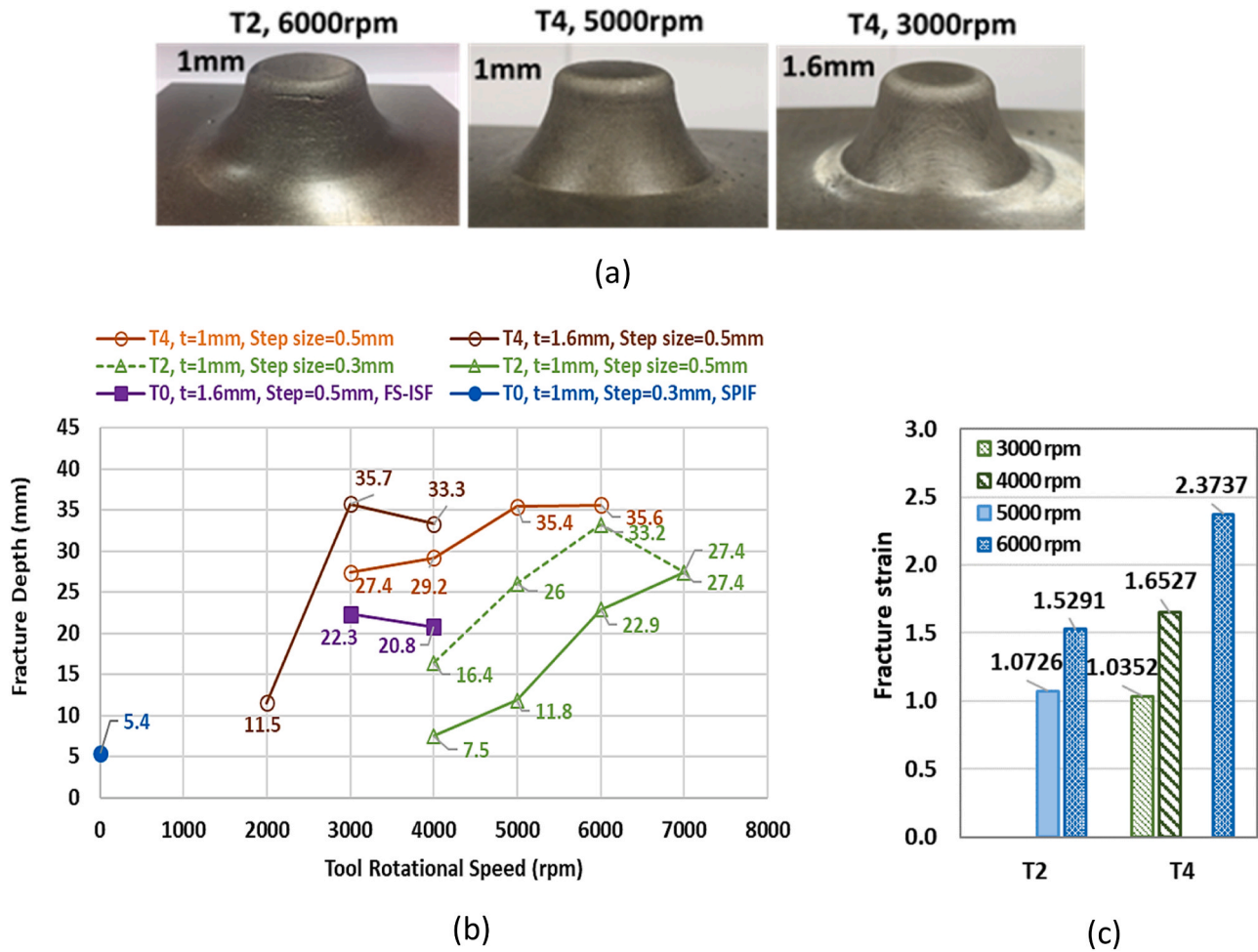| Tool T4 (rosette tool, D=6mm & W=2.5mm)				Tool T2 (double offset = 2 x 1 mm)			
T4 at 2000 rpm		T4 at 3000 rpm		T2 at 2000 rpm		T2 at 3000 rpm	
Reference frequency (Hz) = Number of tool offsets or grooves x Tool rotational speed / 60							
133.33Hz		200Hz		66.67Hz		100Hz	
FE modelled frequencies and amplitudes				FE modelled frequencies and amplitudes			
66.67Hz	133.33Hz	100Hz	200Hz	66.67Hz	133.33Hz	100Hz	200Hz
2.06 m	15.96 m	0.99 m	8.04 m	33.19 m	41.05 m	31.48 m	13.20 m
Measured frequencies and amplitudes				Measured frequencies and amplitudes			
68.36Hz	136.72Hz	103.52Hz	205.08Hz	68.36Hz	136.72Hz	101.56Hz	203.13Hz
1.97 m	11.15 m	2.05 m	4.15 m	81.53 m	31.01 m	64.67 m	18.37 m

Fig. 7. **Formability evaluation of AZ31B hyperbolic cones by T0, T2 and T4.** (a) Samples formed by sheets of thickness of 1 and 1.6 mm; (b) (c) Fracture depths and strains under different rotational speeds.

trend until the end of the process. Due to the relative uniform temperature variations, resulted from a reduced contact area by using the rosette tool thus a reduction of frictional heating, it achieves less sharp reductions of the vertical force following the sheet temperature increases. As a result, the fracture depth has a 60% increase by the RV-ISF than that by the FS-ISF, as shown in Fig. 7b.

3.3. Effects of tool design and rotational speed on tool force and sheet temperature

Fig. 12 shows the time history of peak vertical force and temperature by T2 and T4 when forming the hyperbolic cone under different tool rotational speeds. Both tools produce relatively steady sheet temperature increases and vertical force reductions in the RV-ISF, different from that produced by T0 in the FS-ISF. It is clear that employing T2 produces the highest reduction of the vertical tool force; however, T2 under rotational speed of 4000 and 5000 rpm only produces the maximum peak temperature below 250 °C, while under rotational speed of 7000 rpm, it reaches the maximum value of 350 °C. In contrast, under rotational speed of 5000 and 6000 rpm, T4 achieves the maximum temperature above 400–450 °C, while at 4000 rpm, the sheet temperature maintains at the level of 250 °C after the initial stage of the process. The higher temperatures achieved by T4 may be explained by the greater frequency of the tool-sheet contact by T4 of four grooves than that by T2 of two offsets. Due to higher and stable sheet temperatures achieved by T4, the RV-ISF process enables forming at elevated temperatures of AZ31B sheet to achieve significant formability

improvement, as presented in Section 3.1. Comparing the vertical tool force histories, T2 and T4 produce different force variation patterns, showing that T2 with high vibration amplitudes creates greater vibration effect and greater force reduction earlier in the process than that by T4, as it takes longer for T4 to create vibration effect, depending on groove dimensions. T4 also produces obvious vertical force variations at times between 150–500 s. Although achieving highest vertical force reductions by T2, the sheet fractures earlier at a considerable lower fracture depth than that by T4. It is clear that between the force reduction and temperature increases, the latter plays a more important role in formability improvement.

Fig. 13 shows the time history of peak vertical force and temperature by T2, T3 and T4R when forming the hyperbolic pyramid under different tool rotational speeds. The selection of the different speeds for comparing the tool force and temperature results is because they are the rotational speeds used for achieving the highest fracture depth by each tool, as shown in Fig. 8b. Similar force variation patterns can be observed in forming two different geometries of cone and pyramid by T2 and T4; whilst T2 leads to the biggest reduction of the vertical tool force. T3 with groove depth of 6 mm and width of 2.5 mm causes greater vertical force reductions than that by T4R of a reduced groove depth of 4 mm and width of 2 mm. This indicates that the bigger groove depth, the greater vibration effect of the rosette tool on the deforming sheet, resulting in greater force reduction. From the temperature results, T3 produces a highest temperature increase up to 360 °C at the final stage of the process; while T2 and T4R both maintain a stable temperature around 250 °C but also achieve greater fracture depths. However, T2
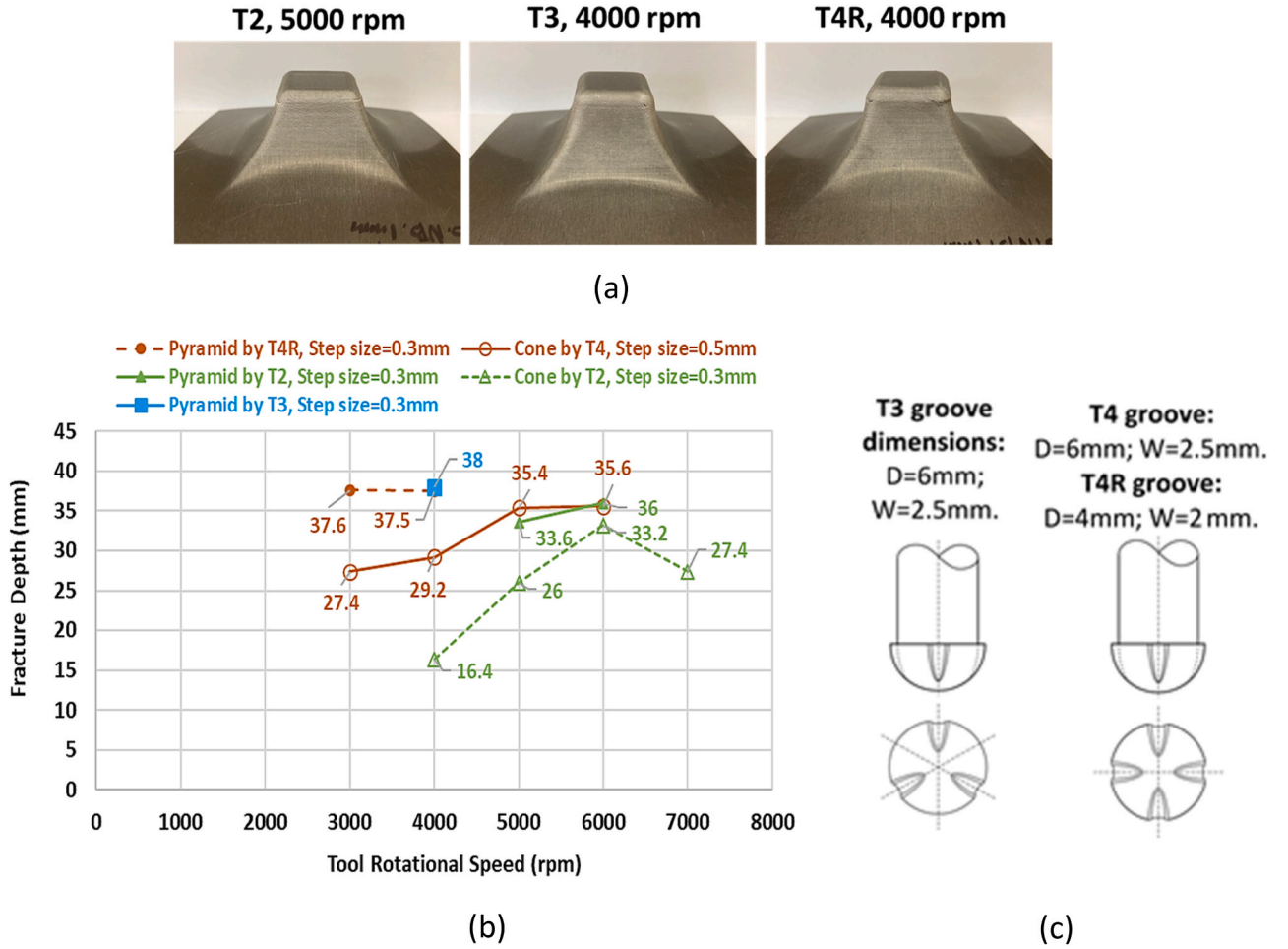
Fig. 8. Formability evaluation of AZ31B hyperbolic pyramids by using T2, T3, and T4R. (a) Pyramid samples formed by sheets of thickness of 1 mm; (b) Comparison of fracture depths of hyperbolic pyramid with that of hyperbolic cones under different conditions; (c) Groove dimensions of rosette tools.

requires higher tool rotational speeds than that by T3 and T4R to improve the fracture depth; this is because T2 has a lower frequency of tool-sheet contact than T3 and T4R under the same tool rotational speed. This indicates both temperature increase and tool-sheet contact frequency are important factors for improving the fracture depth.

The experimental results of the formability study show that significant sheet temperature increases and tool force reductions have occurred in the RV-ISF process; these lead to significant formability improvement of material AZ31B. It is hypothesised that the thermal effect and vibration softening are the key mechanisms for the improved formability of a hard-to-form material in the RV-ISF:

A. Thermal softening due to heat generation created by

- friction due to tool sliding resulted from tool rotation and feeding motion. This effect is similar to that in the FS-ISF but with a reduced degree due to the reduced contact area using the rosette tool;
- plastic deformation of the sheet material and tool-sheet surface cyclic contact under a high strain rate.

B. Vibration softening due to the flow-stress reduction by

- superimposition of the oscillating dynamic load due to tool rotational vibration onto the quasi-static forming load due to tool feeding along ISF tool path;
- dislocations activated by low-frequency and low-amplitude vibration created by rotations of the rosette tool.

4. Discussion of softening mechanisms in the RV-ISF

4.1. Evaluation of thermal effect

Heat generation due to frictional heating and material plastic deformation is essential in increasing the sheet temperature locally to improve the material formability at elevated temperatures. To evaluate effects of various factors on temperature variations in the RV-ISF, the theoretical model of temperature prediction proposed by Giuseppina et al. (2016) for conventional ISF is applied to the RV-ISF process by considering key characteristics of the RV-ISF. In the RV-ISF, the heat generation, Q_{ij}, consists of heating from the plastic deformation, surface friction due to tool rotation speed ω, and tool feed v, these three elements are expressed respectively in Eq. (4). As shown in Fig. 14, by integrating along the meridional direction i and circumferential direction j of the forming geometry respectively, the heat generation over time increment Δt_j can be expressed as:

$$Q_{ij} = \lambda V_{ij}\sigma_{ij}\varepsilon_{ij} + \mu F_{ij}\omega L\Delta t_j + \mu F_{ij}v\Delta t_j \qquad (4)$$

where V_{ij} is the volume of the contact area A_{ij} as analysed in Section 2.1; σ_{ij} is the material flow-stress as a function of the plastic strain ε_{ij}, plastic strain rate $\dot{\varepsilon}_{ij}$ and temperature T_{ij} defined by the J-C model as given in Eq. (3). By applying elementary analysis of the sheet deformation, it can be shown $t_1 = t_0\cos\alpha$, $\varepsilon_{ij} = 2[\ln(t_1/t_0)]/\sqrt{3}$ and $\dot{\varepsilon}_{ij} = [(1-\sin\alpha)/(2\pi)]\Delta t_j$. F_{ij} is the load applied on the contact area by the tool. μ is coefficient of friction and λ is the percentage of the plastic deformation energy transformed to heat. It is assumed that the friction heat generation is
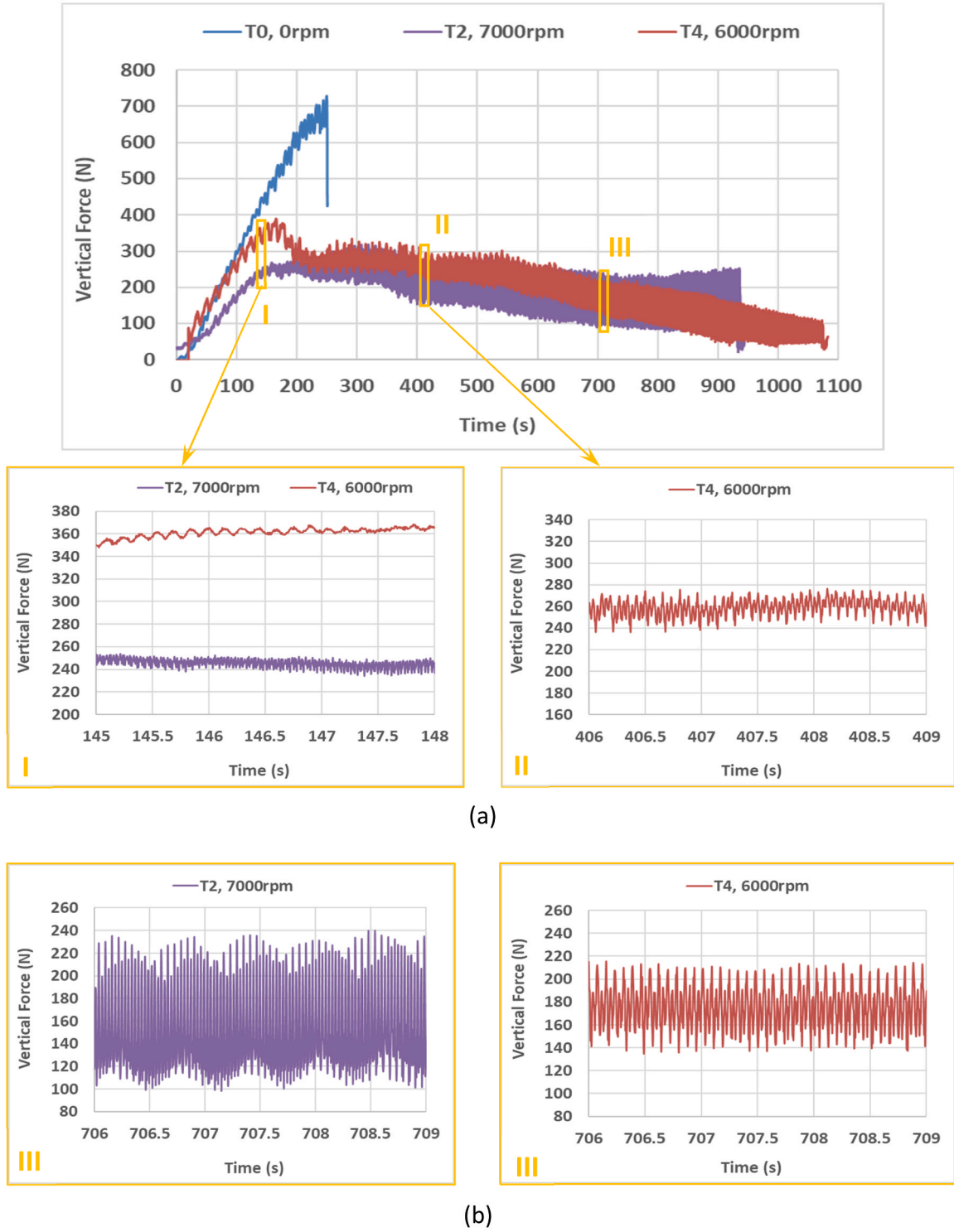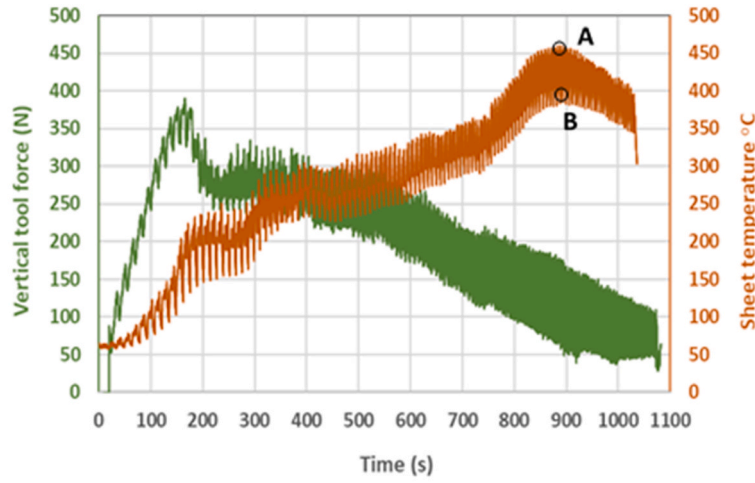
Fig. 9. **Variation of vertical force in forming hyperbolic cones of AZ31B sheet of thickness 1 mm by T2 and T4.** (a) Force-time history during a full RV-ISF process, minor effect of tool vibration at early stages of the process, time I and II; (b) Comparison of force variations using T2 and T4 when a full tool vibration gradually established at the later stage of the process, time III.
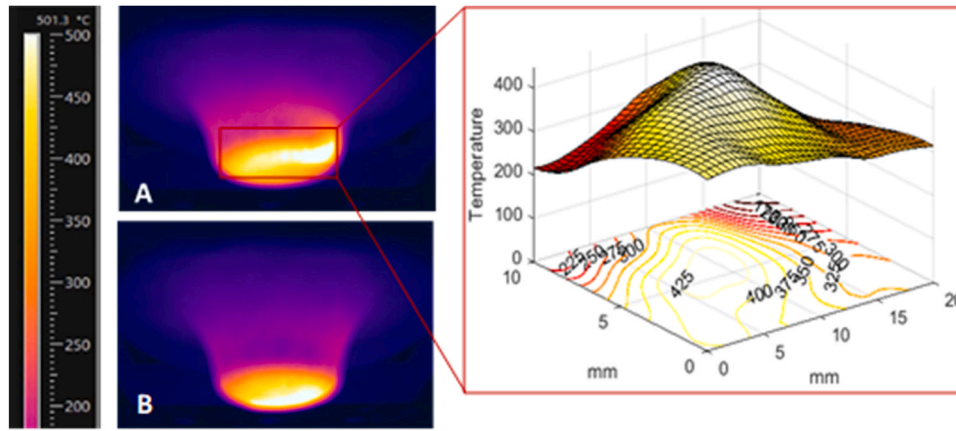
uniform between the tool and deforming sheet, and is equally dissipated into the tool and sheet. Considering heat losses from the heat affected zone, the heat conduction within the sheet blank, Q_{ii}^j can be expressed as

$$Q_{ii}^j = -k_m\left(T_{ij} - T_{ij}\right)/d_{ii}\Delta t_j \tag{5}$$

where d_{ii} is the diameter of the heat affected zone. In this analysis, it is assumed that d_{ii} can be determined by assuming the arc length of the contact area to be equivalent to the heat affected zone, as illustrated in Fig. 14. Heat transfer between sheet and tool, Q_{it}^j, as well as from the sheet to surrounding air, Q_{ia}^j, can be expressed respectively in Eqs. (6) and (7):

Fig. 10. Force and temperature variations in forming a hyperbolic cone using AZ31B sheet of thickness 1 mm by T4 at 6000 rpm. (a) Time history of vertical force and local sheet temperature; (b) Thermal images at tool-sheet contact zone (A) and at non-contact zone (B).
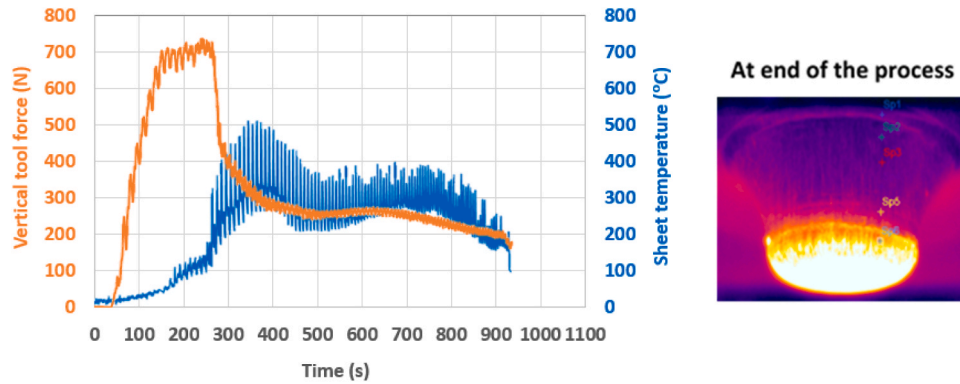

Fig. 11. Time history of vertical forming force and local sheet temperature in forming a hyperbolic cone using AZ31B sheet of thickness 1.6 mm by T0 at 4000 rpm.

$$Q_{it}^j = \frac{T_{ij} - T_a}{\frac{t_1}{k_m A_{ij}} + \frac{r}{k_t A_{ij}}} \Delta t_j \tag{6}$$

$$Q_{ia}^j = h_c \left(T_{ij} - T_a \right) A_{ij} \Delta t_j \tag{7}$$

By combining the elements of heat generation, heat conduction and heat transfer given in the above, the local temperature increase of the deforming sheet can be expressed as

$$\Delta T_{ij} = \frac{Q_{ij} + \sum_j Q_{ii}^j + Q_{it}^j + Q_{ia}^j}{c_p m_{ij}} \tag{8}$$

where m_{ij} is the mass of the contact area. To determine F_{ij}, the measured peak vertical force in forming the hyperbolic pyramid of AZ31B sheet of
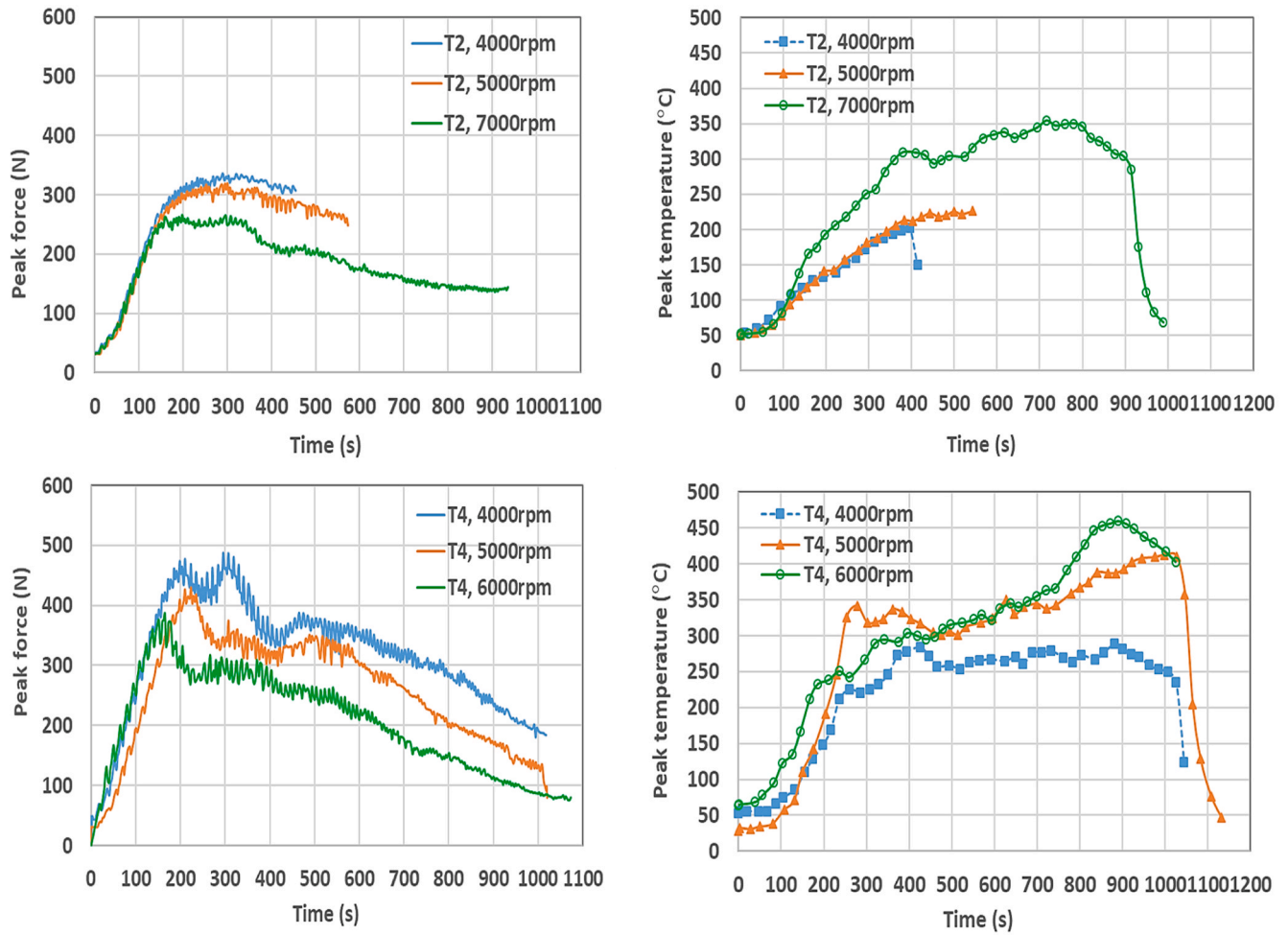
Fig. 12. Peak vertical tool force and sheet temperature in forming hyperbolic cones using AZ31B sheets of thickness 1 mm by T2 and T4.
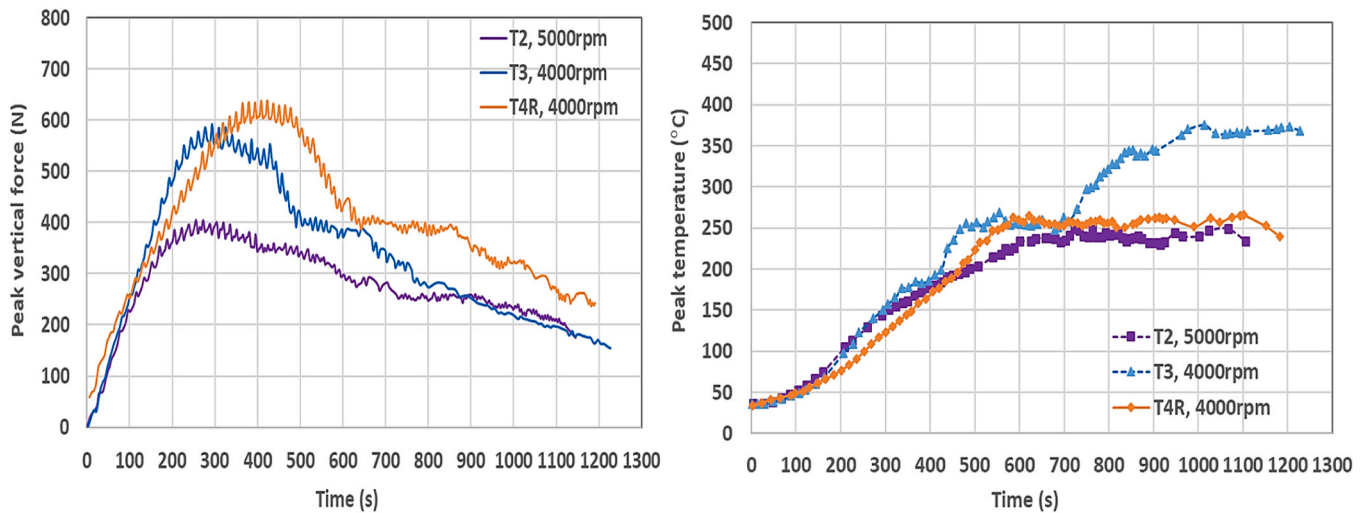

Fig. 13. Peak vertical tool force and sheet temperature in forming hyperbolic pyramids using AZ31B sheets of thickness 1 mm by T2, T3 and T4R.

thickness 1 mm by using T2 and T4R is utilised. The predicted temperature results using Eq. (8) are shown in Fig. 15. The J-C model parameters, material mechanical and thermal properties used in the calculation are listed in Table 3.

Fig. 15a shows that the predicted temperature agrees well with the measured peak temperature in the RV-ISF test by using T4R. To understand the heat generation and heat transfer on temperature variations of the deforming sheet during the RV-ISF, Fig. 15b shows heat gains and losses within the sheet at time 450 s when using the rosette tool T4R. At this stage, the frictional heating is the highest contributor to
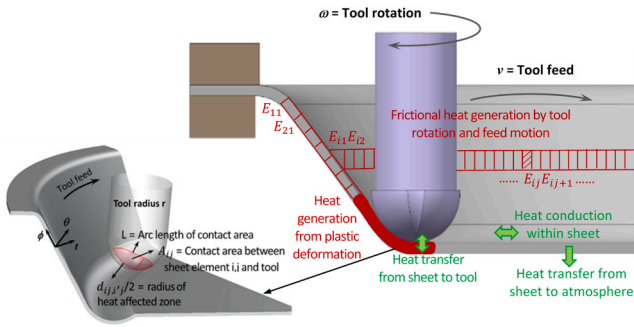
Fig. 14. Temperature prediction model with heat generation from plastic deformation and interfacial friction as well as heat transfer within sheet, between sheet and tool, from sheet to atmosphere.
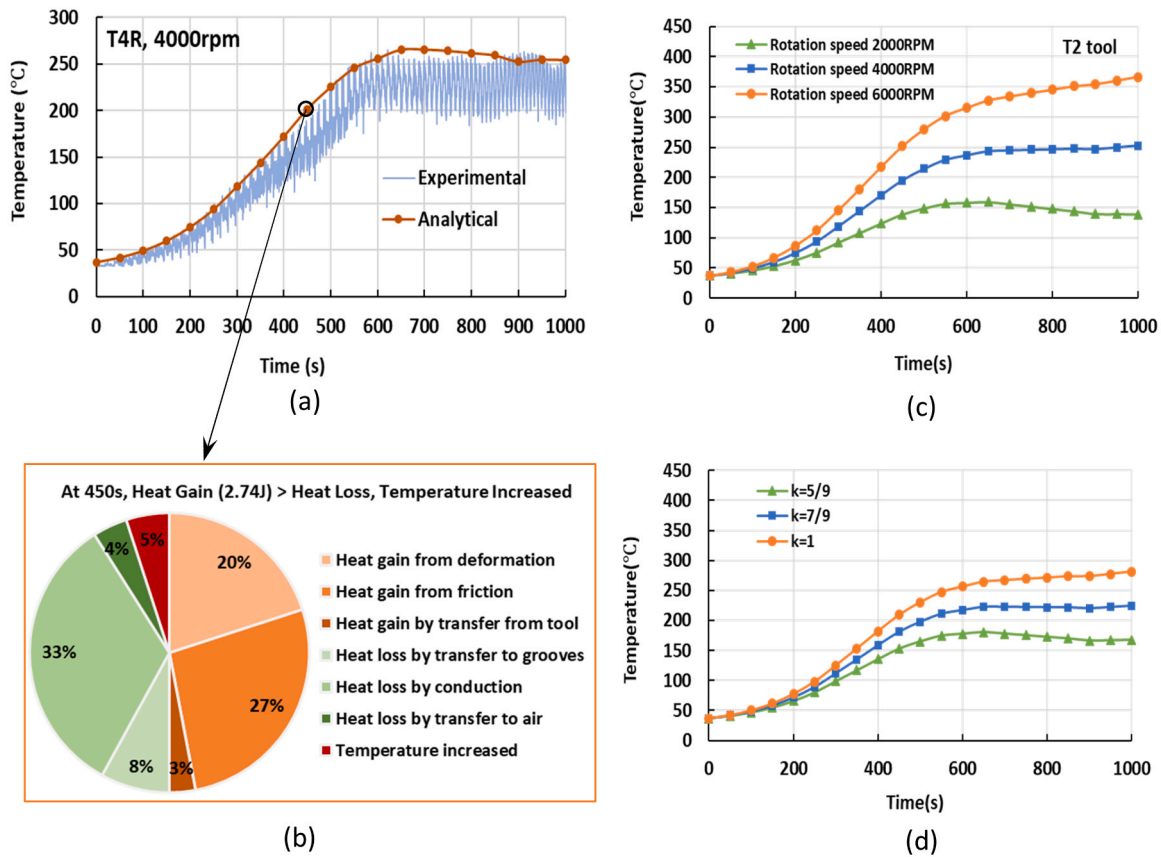
the heat gain, and this is followed by the heat generation from the sheet plastic deformation. Heat conduction within the sheet blank is the main source of heat loss at the heat affected zone. Heat loss by transfer to the grooves of the rosette tool increases with the forming depth and this contributes to the stabilised temperature from the middle to end stages of the process. The interaction of heat generation, conduction and transfer plays an important role in temperature variations of the deforming sheet thus uniquely determines the fracture depth.

A parametric evaluation of temperature increases under different tool rotational speeds is shown in Fig. 15c,d. The tool rotational speed is the most important variable influencing the heat generation, as also observed from the measured temperature results. Tool design is critical to control frictional heating due to its effect on contact area and duration. Fig. 15d compares the temperature increases by varying the contact interval parameter k. For double offset tool T2 and grooved tool T4, as the tool creates periodic surface contacts with the wall of the formed part, the frictional heating is reduced when compared with that in the

Fig. 15. Temperature prediction when forming the AZ31B hyperbolic pyramid in the RV-ISF. (a) Comparison of measured and predicted temperatures based on the measured peak vertical force. (b) Predicted heat grains and heat losses at time 450 s (c) Predicted temperature increases under different rotational speeds by T2. (d) Predicted temperature increases when using different tools at 3000 rpm, k is a parameter to define the tool-sheet contact intervals, for T0, k = 1; T2, k = 5/9; T4, k = 7/9.

Table 3

J-C model parameters, mechanical and thermal properties of AZ31B used in the RV-ISF temperature prediction calculation.

J-C yield strength A (MPa)	J-C hardening coefficient B (MPa)	J-C strain hardening exponent, n	J-C softening exponent, m	Reference strain rate $\dot{\varepsilon}_{ref}$ (s^{-1})	Melting & air temperature T_{melt} & T_a (°C)
172	360	0.456	0.95	0.008	627 & 35

J-C strain rate constant, C	Density ρ(kg/m^3)	Specific heat capacity c_p(J/ (kg K))	Thermal conductivity k_m(W/ (m K))	Convection coefficient h_c(W/(m^2 K))	Coefficient of friction μ
0.092	1800	1000	96	1000	0.15

FS-ISF using T0. Under the same tool rotational speed, the contact area of different tools is also different, depending on the dimensions of groove or offset design along the tool circumference. Both lead to differences in frictional heat generation in the RV-ISF process.

By conducting comprehensive RV-ISF experimental tests under various process conditions, it has been observed that each tool design requires a different range of the rotational speed to achieve greater temperature increases. T4 tools require lower rotational speeds than that by T2 and T3 to achieve formability improvement because of its greater tool-sheet contact frequency. However, if the rotational speed employed is too high and beyond a specific speed limit for a tool, the sheet will fail at a reduced fracture depth. The results obtained from the experiment and prediction have also suggested that maintaining a stable temperature condition is the main factor for the formability improvement while the vibration has a greater effect on the forming force reduction in the RV-ISF. The effects of the vibration amplitude and frequency on vibration softening is discussed in the following section.

4.2. Evaluation of vibration softening

As observed by Langenecker (1966) and discussed by Yao et al. (2012) and Zhou et al. (2018), the vibration softening takes its effects through stress superimposition and dislocation activation to reduce the material flow-stress thus improving the formability. In the RV-ISF, the oscillating dynamic loading due to the rotational vibration by the rosette tool can cause the flow-stress reduction by stress superimposition and dislocation activation. Yao et al. (2012) and Wang et al. (2016) proposed an analytical method to quantify the vibration softening in the ultrasonic vibration-assisted uniaxial tension. By applying the analytical method proposed in their studies, the material flow-stress reduction in the RV-ISF, $\Delta\sigma$, caused by vibration softening can be considered as a combination of stress superimposition, $\Delta\sigma_{SU}$, and dislocation activation by vibration energy, $\Delta\sigma_V$

$$\Delta\sigma = \Delta\sigma_{SU} + \Delta\sigma_V \tag{9}$$

$$\Delta\sigma_{SU} = -K\xi_{eq}^n \tag{10}$$

$$\Delta\sigma_V = -\beta M\widehat{\tau}\left(\frac{\overline{E}}{\widehat{\tau}}\right)^m \quad where \quad \overline{E} = \gamma\rho\xi_{eq}^2\omega_{eq}^2 \tag{11}$$

where ξ_{eq} and ω_{eq} are the equivalent vibration amplitude and angular frequency respectively; ρ is the material density; K is the strength coefficient and n is the hardening exponent of the material. γ is a geometrical constant in calculating the equivalent polar moment of inertia of a specific geometry of the tool, it can be derived that $\gamma = 0.2$ for T2 tool and 0.5 for T4 tool. $\overline{E}$ is the vibration energy density, $\widehat{\tau}$ is the mechanical threshold for activating dislocation of a given material; M is the Taylor factor, β and m are parameters to be found by experiments. To quantify the effect of the vibration activated dislocation, these key parameters need to be determined experimentally, as investigated by Yao et al. (2012) and Wang et al. (2016). From these previous studies, it is clear that the vibration softening is influenced by both amplitude and frequency of the vibration. However, based on the RV-ISF experimental data in this study, it is only possible to qualitatively evaluate the effect of the vibration softening.

To evaluate effect of the stress superimposition and vibration energy on the flow-stress reduction, $\Delta\sigma_{SU}$ and $\Delta\sigma_V$ are calculated by determining the equivalent vibration amplitude and frequency:

$$\xi_{eq} = \kappa\xi_1 + (1-\kappa)\xi_2 \quad and \quad \omega_{eq} = \kappa\omega_1 + (1-\kappa)\omega_2 \tag{12}$$

where ξ_1 and ξ_2 are vibration amplitudes at two most dominating vibration frequencies ω_1 and ω_2 measured in the experiment, as shown in Table 2. The equivalent vibration amplitude ξ_{eq} and frequency ω_{eq} are determined by selecting a parameter κ, the proportional percentage of two vibration peaks contributing to the equivalent values as defined in

Eq. (12). Based on the experimental measured vibration data presented in Table 2 and by varying κ as 1 and 0.5 respectively, Fig. 16 shows the predicted flow-stress reduction due to stress superimposition, $\Delta\sigma_{SU}$, and vibration energy for activating dislocation, $\Delta\sigma_V$, respectively. The values of the parameters used in the calculations are $K = 324$ MPa and $n = 0.14$ from Jaimin et al. (2023), $M = 3.06$, $\beta = 207.9$, $m = 0.5$ and $\widehat{\tau} = 138$ MPa from Yao et al. (2012). From the predicted results, it can be observed that the flow-stress reduction due to stress superimposition is greater than that due to the effect of vibration energy activated dislocations, which agrees with the experimental observation of the vertical force reduction discussed in Section 3.3. The vibration amplitude, in comparison with the vibration frequency, has a greater effect on the stress reduction; T2 tool with a greater amplitude of 18–80 μm has a greater effect than that by T4 of a small amplitude of 2–11 μm.

At the same temperature and strain rate, the flow-stress behaviour of magnesium alloy AZ31B is influenced by average dislocation density, which is decreasing due to dynamic recovery and dynamic recrystallization, but increasing due to work hardening. As discussed by Chen et al. (2019), before dynamic recrystallization, the flow-stress increases with the increasing strain because the average dislocation density increases under the combined effect of work hardening and dynamic recovery. When the average dislocation density reaches a critical value, dynamic recrystallization will be initiated. Under the combined effect of work hardening, dynamic recovery and dynamic recrystallization, the flow-stress will gradually decrease, and may reach a steady state when a balance is reached among these three conditions. To ascertain if the rotational vibration condition in the RV-ISF has activated dislocations and dynamic recrystallization, the following section evaluates the microstructure evolution of samples cut from the formed AZ31B hyperbolic cones and the EBSD scanning of the samples is performed.

4.3. Analysis of microstructural evolution

Fig. 17a illustrates the location of sheet samples cut from the AZ31B hyperbolic cones obtained in the RV-ISF formability experiment for the EBSD analysis. Fig. 17b shows the average grain size and proportion of low-angle grain boundaries (LAGBs) vs. measured micro hardness of the samples. Fig. 17c-e show grain distributions and inverse pole figure (IPF) maps. Fig. 18 shows Kernel Average Misorientation (KAM) distribution and area fraction of misorientation angles of the microstructure as-received, formed by T2 and T4 under rotational speed 6000 rpm, respectively. It can be observed that grain sizes of the microstructure after RV-ISF are reduced from the as-received. The average grain sizes formed by T2 and T4 are similar, approximately 2.7 μm. Fig. 18 also shows considerable grain rotations by T4; however, the proportion of LAGBs produced by using T2 with larger vibration amplitudes is smaller than that by T4 with lower vibration amplitudes. The KAM distribution by T2 is smaller than that by T4, indicating that the dislocation density by T2 is lower.

A visible delamination of grain orientations can be observed in the grain distribution map by using T2, as shown in Fig. 17d. This is because the low-frequency vibration created by T2 has a limited transmission capacity in the sheet thickness direction. Therefore, the grains close to the tool-sheet contact surface are easier to rotate under the effect of vibration energy and large shear stresses. The orientation of grains near the tool-sheet contact surface has changed significantly by high vibration amplitudes using T2, and the LAGBs are gradually transformed to high-angle grain boundaries. On the other hand, through-thickness microstructure transformation can be observed in the microstructure produced by T4, as shown in Fig. 17e. This can be resulted from higher dislocation density and higher temperature generated by T4 than that by T2, leading to the activation of dynamic recrystallization in the microstructure produced by T4. This observation agrees with the findings by Siu et al. (2011), that the enhanced subgrain formation by the ultrasound vibration was proved to be a lot greater than that due to the heat that it generated within the metal. As shown in Fig. 17, the IPF map of
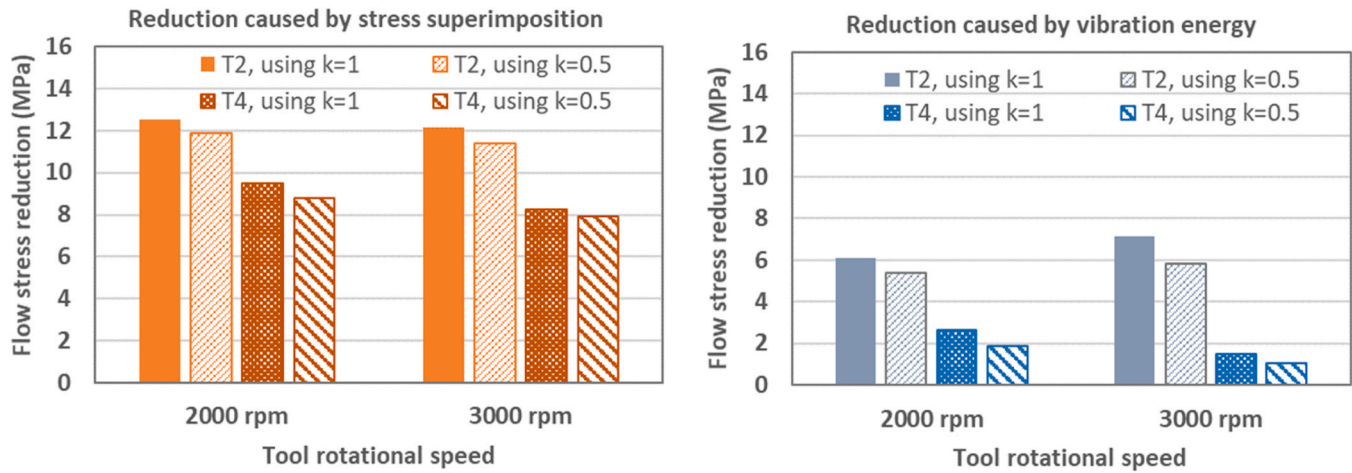
Fig. 16. Predicted flow-stress reductions caused by stress superimposition $\Delta\sigma_{SU}$ and vibration energy $\Delta\sigma_V$ respectively, using the experimental measured amplitudes and frequencies.

the as-received microstructure has a strong texture in base {0001}; the pole density centre is along the normal direction, while the texture components in {10−10} and {11−20} are weak. Because the dynamic recrystallization has been activated by T4, the pole density centre gradually rotates from the normal direction to the rolling direction, resulting in the change of grain orientations and texture directions. The microstructure produced by T2 does not show an obvious dynamic recrystallization, and the effects of the surface shear stress and vibration field have not changed the texture orientation, however, they have caused a decrease of small grain misorientation angles. In addition, an obvious bimodal structure of the pole density in base plane {0001} could be considered to be caused by the twinning in the {11−20} plane, indicating that there are abundant deformation twins in the AZ31B samples under the effect of severe plastic deformation by using T4 with low vibration amplitudes in the RV-ISF.

The elevated temperature and low-frequency vibration created by using T2 and T4 have resulted in enhanced micro hardness of the microstructure. Fig. 17b compares the proportion of the LAGBs with the measured micro hardness results of the samples. It is observed that the RV-ISF with low-frequency vibrations using either T2 (high amplitudes) or T4 (low amplitudes) has improved the micro hardness when compared with that of the as-received material. The micro hardness is further enhanced when using the T2 tool with higher vibration amplitudes in the RV-ISF.

In summary, the evaluation and analysis in this section have shown that the thermal and vibration softening mechanisms are the main contributors to the formability improvement in the RV-ISF. The thermal softening is achieved by heat generation from interfacial friction and plastic deformation while the vibration softening is attained by the flow-stress reduction through the stress superimposition and activated dislocations by using the rosette tool in the RV-ISF, both enhance the formability. Furthermore, the severe plastic deformation in the RV-ISF has produced the refined grain structures and increased micro hardness of the AZ31B samples. The additional effect of the low-frequency and low-amplitude vibration created by the tool rotation using the novel rosette tool design T4 in the RV-ISF process has achieved the elevated temperature of 250–450 °C, resulted in higher proportion of LAGBs and dislocation density, and the activation of dynamic recrystallization, significantly enhancing the formability of a hard-to-form material.

5. Conclusions

The aim of this study is to develop a new rotational vibration assisted ISF (RV-ISF) process by employing a novel type of rosette tool design to improve the material formability. By investigating the capability of the RV-ISF in processing magnesium alloy AZ31B, the mechanisms of the thermal effect and vibration softening on the formability enhancement are investigated. The following conclusions may be drawn:

1) By developing the rosette tools for the first time, low-frequency and low-amplitude vibrations of the deforming sheet have been created, in the range of 67–400 Hz and 2–11 μm respectively by tool T4, to enable rotational vibration-assisted ISF of a hard-to-form material, without the need of using additional systems or devices. Double offset tool T2 has created much higher vibration amplitudes in the range of 18–80 μm.

2) By using the rosette tools, the RV-ISF has attained elevated temperatures in the range of 250–450 °C, leading to a significant formability improvement of the material. It has shown a 60% increase of fracture depth than that by the FS-ISF when forming hyperbolic cones by using T4 tool. Greater fracture depths are obtained in forming hyperbolic pyramids than that in forming hyperbolic cones, indicating that the RV-ISF is capable of achieving higher formability under multiaxial stress conditions.

3) Considerable reductions of the vertical forming force, more than 46%, are observed by using rosette tools of T2, T3, T4 and T4R in the RV-ISF than that in the conventional ISF. T2 tool with higher vibration amplitudes results in the highest reduction of the vertical forming force. T3, T4 and T4R tools with smaller vibration amplitudes have maintained stable temperature increases and attained the lowest vertical force at the later stage of the RV-ISF process, achieving highest fracture depths.

4) The RV-ISF of AZ31B sheets by using T4 tool has activated microstructure dislocations and dynamic recrystallization, and produced refined microstructural grains, considerable grain rotations and increased micro hardness. The microstructure produced by T2 tool has shown a lower degree of dislocations but no obvious dynamic recrystallization observed. However, micro hardness by T2 tool is higher than that by T4 tool owing to much higher vibration amplitudes created by T2 tool.

5) The combined thermal effect and vibration softening is the key mechanism leading to the significant formability enhancement. The rosette tool design has a critical effect on both frictional heating as well as vibration frequency and amplitude, while the tool rotational speed is the most important process variable influencing frictional heating and vibration frequency. With a higher vibration frequency and longer tool-sheet contact duration, it increases frictional heating, enhancing thermal softening. The groove dimensions of the rosette tool affect vibration amplitudes and the number of grooves of the
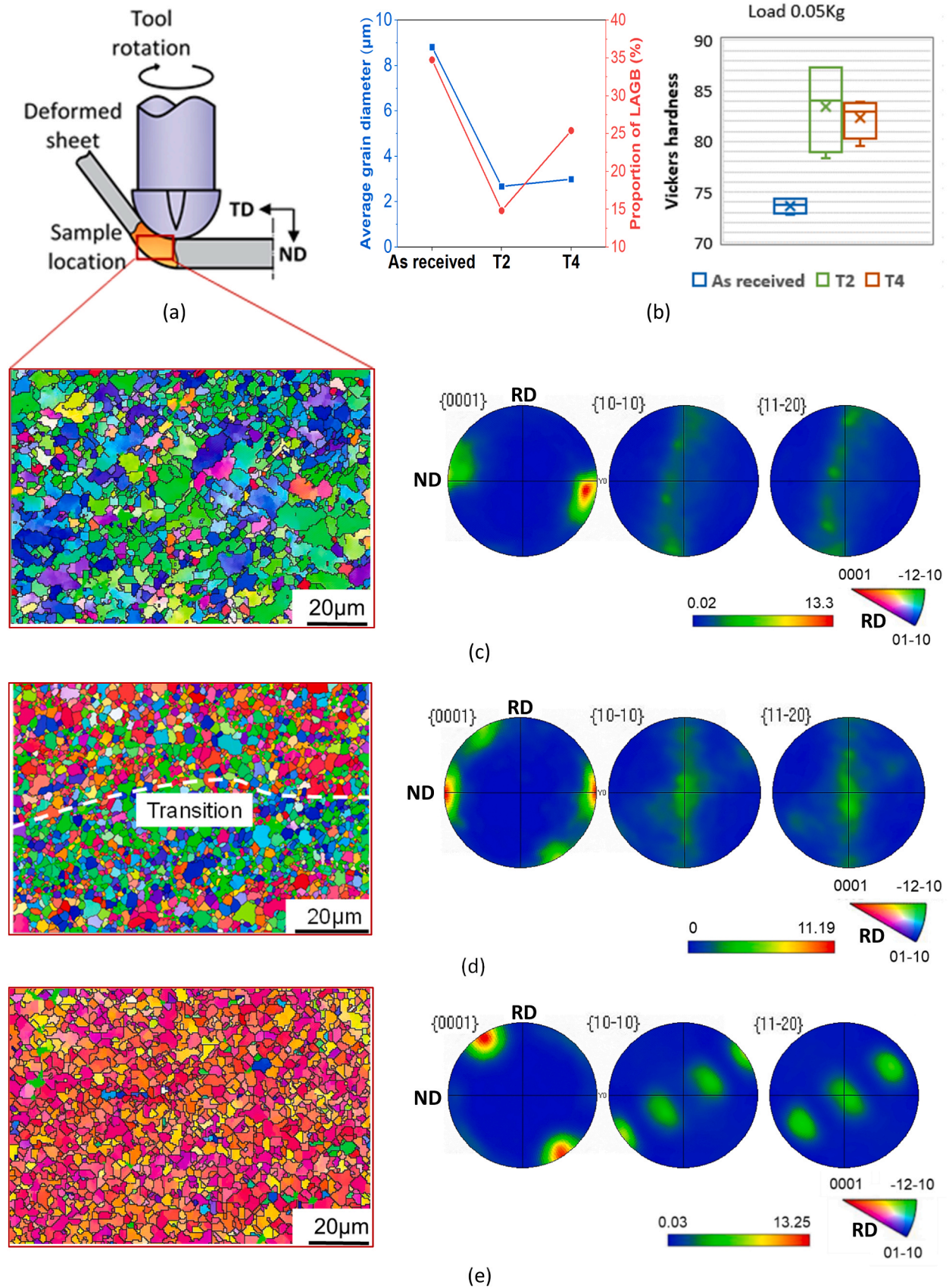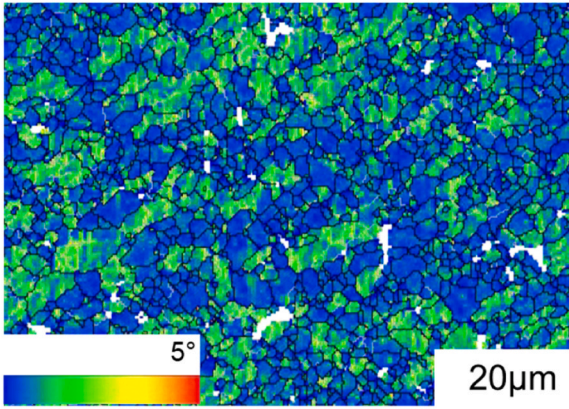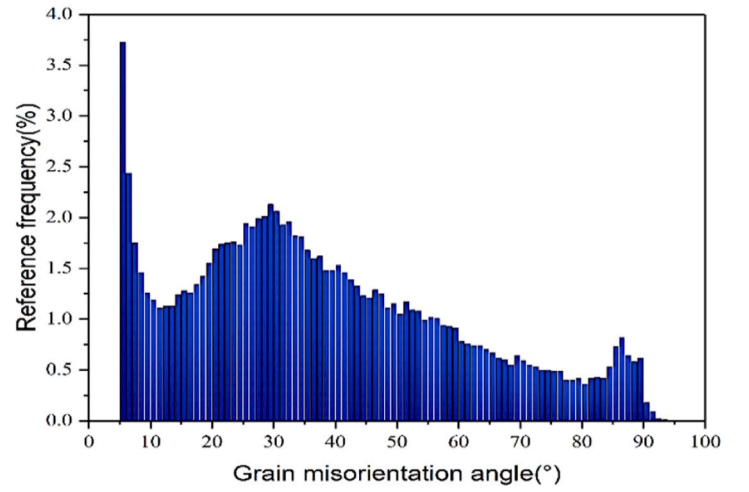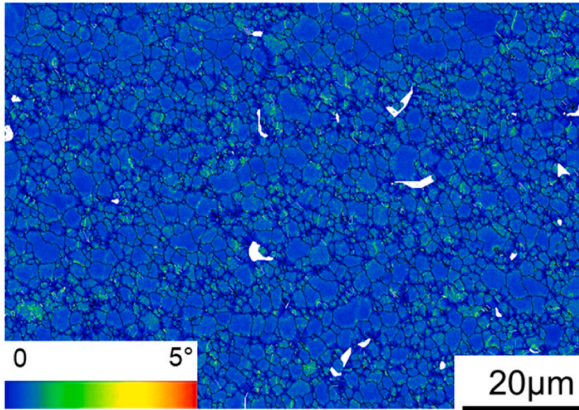
Fig. 17. **Evaluation of EBSD scanned samples cutting from the AZ31B hyperbolic cones formed by RV-ISF.** (a) Sample location; (b) Proportion of LAGBs vs. micro hardness; (c), (d) and (e) Grain distribution and EBSD inverse pole figure maps: as-received, produced by T2 and T4 under rotational speed of 6000 rpm.
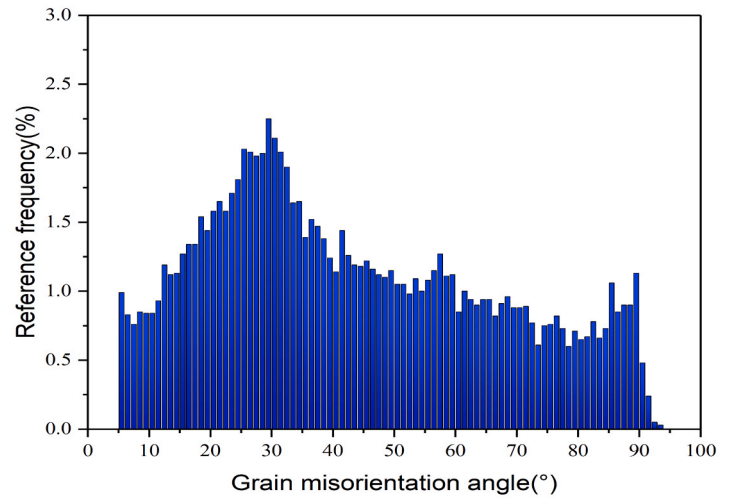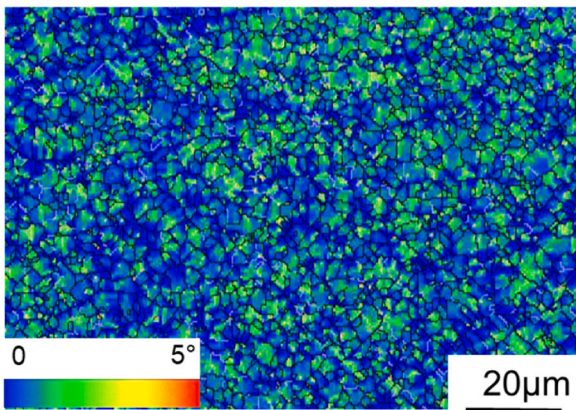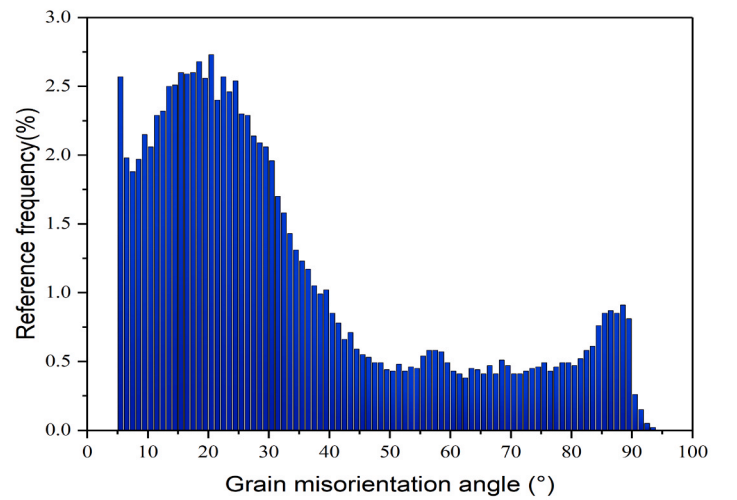
(a)

(b)

(c)

(d)

(e)

(f)

Fig. 18. Kernel Average Misorientation (KAM) and area fraction of misorientation angles of samples from AZ31B hyperbolic cone. (a) & (b) As-received, (c) & (d) and (e) & (f) produced by T2 and T4 under rotational speed of 6000 rpm, respectively.

rosette tool determines vibration frequencies, thus both are critical to vibration softening.

6) Analytical prediction of the flow-stress reduction due to vibration softening shows that the effect from the stress superimposition is greater than that from the vibration activated dislocations. Further investigations to quantify the effect of vibration softening can advance the current understanding for developing vibration-assisted sheet forming technologies. Future studies on optimisation of the rosette tool design and selection of the key process parameters in the RV-ISF can lead to the realisation of its full potential to improve the formability when processing different types of materials and complex geometries in manufacture sheet metal products.

CRediT authorship contribution statement

Long Hui: Writing – review & editing, Writing – original draft, Validation, Supervision, Methodology, Funding acquisition, Formal analysis, Conceptualization. **Peng W.X.:** Writing – review & editing, Visualization, Validation, Methodology, Investigation, Formal analysis. **Chang Z.D.:** Writing – review & editing, Visualization, Validation, Methodology, Investigation, Formal analysis. **Zhu H.:** Writing – review & editing, Visualization, Methodology, Investigation, Formal analysis. **Jiang Y.J.:** Investigation. **Li Z.H.:** Investigation.

Declaration of Competing Interest

The authors declare that there is no conflict of interests regarding the publication of this work.

Acknowledgments

References

Ambrogio, G., Filice, L., Manco, G.L., 2008. Warm incremental forming of magnesium alloy AZ31. CIRP Ann. - Manuf. Technol. 57, 257–260. https://doi.org/10.1016/j.cirp.2008.03.066.

Amini, S., Hosseinpour Gollo, A., Paktinat, H., 2017. An investigation of conventional and ultrasonic-assisted incremental forming of annealed AA1050 sheet. Int. J. Adv. Manuf. Technol. 90, 1569–1578. https://doi.org/10.1007/s00170-016-9458-7.

Amini, S., Nazari, F., Baraheni, M., Ghasemi, A.H., 2018. Investigating the effect of rotation speed and ultrasonic vibrations in the incremental forming process. Int. J. Adv. Des. Manuf. Technol. 11 (4), 91–97. https://admt.isfahan.iau.ir/article_668322.html.

Attanasio, A., Ceretti, E., Giardini, C., Mazzoni, L., 2008. Asymmetric two points incremental forming: Improving surface quality and geometric accuracy by tool path optimization. J. Mater. Process. Technol. 197 (1-3), 59–67. https://doi.org/10.1016/j.jmatprotec.2007.05.053.

Blaha, F., Langenecker, B., 1959. Ultrasonic investigation of the plasticity of metal crystals. Acta Metall. 7, 93–100. https://doi.org/10.1016/0001-6160(59)90114-2.

Chang, Z., Li, M., Chen, J., 2019. Analytical modelling and experimental validation of the forming force in several typical incremental sheet forming processes. Int. J. Mach. Tools Manuf. 140, 62–76. https://doi.org/10.1016/j.ijmachtools.2019.03.003.

Chen, M.S., Yuan, W.Q., Li, H.B., Zou, Z.H., 2019. New insights on the relationship between flow stress softening and dynamic recrystallization behaviour of magnesium alloy AZ31B. Mater. Charact. 147, 173–183. https://doi.org/10.1016/j.matchar.2018.10.031.

Cheng, R., Wiley, N., Short, M., Liu, X., Taub, A., 2019. Applying ultrasonic vibration during single-point and two-point incremental sheet forming. Procedia Manuf. 34, 186–192. https://doi.org/10.1016/j.promfg.2019.06.137.

Cheng, Z., Li, Y.L., Li, J.H., Li, F.Y., Meehan, P.A., 2022. Ultrasonic assisted incremental sheet forming: constitutive modelling and deformation analysis. J. Mater. Process. Tech. 299, 117365 https://doi.org/10.1016/j.jmatprotec.2021.117365.

Cooper, D.R., Gutowski, T.G., 2020. Prospective environmental analyses of emerging technology: a critique, a proposed methodology, and a case study on incremental sheet forming. J. Ind. Ecol. 24, 38–51. https://doi.org/10.1111/jiec.12748.

Duflou, J.R., Callebaut, B., Verbert, J., De Baerdemaeker, H., 2007. Laser assisted incremental forming: formability and accuracy improvement. CIRP Ann. Manuf. Technol. 56, 273–276. https://doi.org/10.1016/j.cirp.2007.05.063.

Duflou, J.R., Habraken, A.-M., Cao, J., Malhotra, R., Bambach, M., Adams, D., Vanhove, H., Mohammadi, A., Jeswiet, J., 2018. Single point incremental forming: state-of-the-art and prospects. Int. J. Mater. Form. 11, 743–773. https://doi.org/10.1007/s12289-017-1387-y.

Emmens, W.C., Sebastiani, G., van den Boogaard, A.H., 2010. The technology of incremental sheet forming - a brief review of the history. J. Mater. Process. Technol. 210, 981–997. https://doi.org/10.1016/j.jmatprotec.2010.02.014.

Fan, G., Gao, L., Hussain, G., Wu, Z., 2008. Electric hot incremental forming: a novel technique. Int. J. Mach. Tools Manuf. 48, 1688–1692. https://doi.org/10.1016/j.ijmachtools.2008.07.010.

Giuseppina, A., Claudio, C., Luigino, F., Francesco, G., 2016. Theoretical model for temperature prediction in incremental sheet forming-experimental validation. Int. J. Mech. Sci. 39–48. https://doi.org/10.1016/j.ijmecsci.2016.01.030.

Green, R.E., 1975. Non-linear effects of high-power ultrasonics in crystalline solids. Ultrasonics 13, 117–127. https://doi.org/10.1016/0041-624X(75)90063-3.

Hirt, G., Kordtomeikel, R., Bremen, T., Laugwitz, M., Bailly, D., 2021. On the geometrical accuracy in incremental sheet forming, forming the future. Miner., Met. Mater. Ser. Book Ser. (MMMS) 507–521. https://doi.org/10.1007/978-3-030-75381-8_42.

Huang, H., Pequegnat, A., Chang, B., Mayer, M., Du, D., Zhou, Y., 2009. Influence of superimposed ultrasound on deformability of Cu. J. Appl. Phys. 106, 113514 https://doi.org/10.1063/1.3266170.

Jaimin, A., Kotkunde, N., Sadhukhan, A., Anand, A.J., Morchhale, A., Singh, S.K., 2023. Flow stress and work hardening behaviour of Mg-3Al-1Zn alloy. Proc. IMechE Part E: J. Process Mech. Eng. 237 (3), 719–730. https://doi.org/10.1177/09544089221106970.

Langenecker, B., 1961. Work-softening of metal crystals by alternating the rate of glide strain. Acta Metall. 9 (10), 937–940. https://doi.org/10.1016/0001-6160(61)90112-2.

Langenecker, B., 1966. Effects of ultrasound on deformation characteristics of metals. IEEE Trans. Sonics Ultrason. 13 (1), 1–8. https://doi.org/10.1109/T-SU.1966.29367.

Li, P., He, J., Liu, Q., Yang, M., Wang, Q., Yuan, Q., Li, Y., 2017a. Evaluation of forming forces in ultrasonic incremental sheet metal forming. Aerosp. Sci. Technol. 63, 132–139. https://doi.org/10.1016/j.ast.2016.12.028.

Li, Y.L., Chen, X.X., Sun, J., Li, J.F., Zhao, G.Q., 2017b. Effects of ultrasonic vibration on deformation mechanism of incremental point-forming process. Procedia Eng. 207, 777–782. https://doi.org/10.1016/j.proeng.2017.10.828.

Long, Y., Li, Y., Sun, J., Ille, I., Li, J., Twiefel, J., 2018. Effects of process parameters on force reduction and temperature variation during ultrasonic assisted incremental sheet forming process. Int. J. Adv. Manuf. Technol. 97, 13–24. https://doi.org/10.1007/s00170-018-1886-0.

Lu, B., Fang, Y., Xu, D., Chen, J., Ou, H., Moser, N.H., Cao, J., 2014. Mechanism investigation of friction-related effects in single point incremental forming using a developed oblique roller-ball tool. Int. J. Mach. Tools Manuf. 85, 14–29. https://doi.org/10.1016/j.ijmachtools.2014.04.007.

Lu, B., Li, Z., Long, H., Chen, F., Chen, J., Ou, H., 2017. Microstructure refinement by tool rotation-induced vibration in incremental sheet forming. Procedia Eng. 207, 795–800. https://doi.org/10.1016/j.proeng.2017.10.831.

Lum, I., Huang, H., Chang, B., Mayer, M., Du, D., Zhou, Y., 2009. Effects of superimposed ultrasound on deformation of gold. J. Appl. Phys. 105, 024905 https://doi.org/10.1063/1.3068352.

Nasulea, D., Oancea, G., 2021. Achieving accuracy improvements for single-point incremental forming process using a circumferential hammering tool. Metals 11, 482. https://doi.org/10.3390/met11030482.

Otsu, M., Matsuo, H., Matsuda, M., Takashima, K., 2010. Friction stir incremental forming of aluminium alloy sheets. Steel Res. Int. 81 (9), 942–945.

Otsu, M., Ichikawa, T., Matsuda, M., Takashima, K., 2011. Improvement of formability of magnesium alloy sheets by friction stir incremental forming. Steel Res. Int. Spec. Ed. 537–541.

Otsu, M., Yasunaga, M., Matsuda, M., Takashima, K., 2014. Friction stir incremental forming of A2017 aluminium sheets. Procedia Eng. 81, 2318–2323. https://doi.org/10.1016/j.proeng.2014.10.327.

Pohlman, R., Lehfeldt, E., 1966. Influence of ultrasonic vibration on metallic friction. Ultrasonics 4, 178–185. https://doi.org/10.1016/0041-624X(66)90244-7.

Sedaghat, H., Xu, W., Zhang, L., 2019. Ultrasonic vibration-assisted metal forming: constitutive modelling of acoustoplasticity and applications. J. Mater. Process. Technol. 265, 122–129. https://doi.org/10.1016/j.jmatprotec.2018.10.012.

Siu, K.W., Ngan, A.H.W., Jones, I.P., 2011. New insight on acoustoplasticity – ultrasonic irradiation enhances subgrain formation during deformation. Int. J. Plast. 27, 788–800. https://doi.org/10.1016/j.ijplas.2010.09.007.

Vahdati, M., Mahdavinejad, R., Amini, S., 2017. Investigation of the ultrasonic vibration effect in incremental sheet metal forming process. Proc. IMechE Part B: J. Eng. Manuf. 231, 971–982. https://doi.org/10.1016/j.proeng.2017.10.828.

Wang, C.J., Liu, Y., Guo, B., et al., 2016. Acoustic softening and stress superposition in ultrasonic vibration assisted uniaxial tension of copper foil: experiments and modelling. Mater. Des. 112, 246–253. https://doi.org/10.1016/j.matdes.2016.09.042.

Wang, Z.H., Cai, S., Chen, J., 2020. Experimental investigations on friction stir assisted single point incremental forming of low-ductility aluminium alloy sheet for higher

formability with reasonable surface quality. J. Mater. Process. Tech. 277, 116488 https://doi.org/10.1016/j.jmatprotec.2019.116488.

Wu, S., Geng, P., Ma, N., Lu, F., 2022. Contact-induced vibration tool in incremental sheet forming for formability improvement of aluminium sheets. J. Mater. Res. Technol. 17, 1363–1379. https://doi.org/10.1016/j.jmrt.2022.01.103.

Xiao, X., Oh, S.H., Kim, S.H., Kim, Y.S., 2022. Effects of low-frequency vibrations on single point incremental sheet form. Metals 12 (2), 346. https://doi.org/10.3390/met12020346.

Xu, D., Wu, W., Malhotra, R., Chen, J., Lu, B., Cao, J., 2013. Mechanism investigation for the influence of tool rotation and laser surface texturing (LST) on formability in single point incremental forming. Int. J. Mach. Tools Manuf. 73, 37–46. https://doi.org/10.1016/j.ijmachtools.2013.06.007.

Xu, D., Lu, B., Cao, T., Chen, J., Long, H., Cao, J., 2014. A comparative study on process potentials for frictional stir- and electric hot-assisted incremental sheet forming. Procedia Eng. 81, 2324–2329. https://doi.org/10.1016/j.proeng.2014.10.328.

Xu, D.K., Lu, B., Cao, T.T., Zhang, H., Chen, J., Long, H., Cao, J., 2016. Enhancement of process capabilities in electrically-assisted double sided incremental forming. Mater. Des. 92, 268–280. https://doi.org/10.1016/j.matdes.2015.12.009.

Yang, M., Bai, L., Li, Y., Yuan, Q., 2019. Influences of vibration parameters on formability of 1060 aluminium sheet processed by ultrasonic VA single point incremental forming. Adv. Mater. Sci. Eng., 8405438 https://doi.org/10.1155/2019/8405438.

Yao, Z., Kim, G.Y., Wang, Z., Faidley, L.A., Zou, Q., Mei, D., Chen, Z., 2012. Acoustic softening and residual hardening in aluminium: Modelling and experiments. Int. J. Plast. 39, 75–87. https://doi.org/10.1016/j.ijplas.2012.06.003.

Zhang, L., Wu, C., Sedaghat, H., 2021. Ultrasonic vibration–assisted incremental sheet metal forming. Int. J. Adv. Manuf. Techno. 114, 3311–3323. http://link.springer.com/article/10.1007/s00170-021-07068-5.

Zhou, H., Cui, H., Qin, Q.H., Wang, H., Shen, Y., 2017. A comparative study of mechanical and microstructural characteristics of aluminium and titanium undergoing ultrasonic assisted compression testing. Mater. Sci. Eng. A 682, 376–388. https://doi.org/10.1016/j.msea.2016.11.021.

Zhou, H, Cui, H., Qin, Q.H., 2018. Influence of ultrasonic vibration on the plasticity of metals during compression process. J. Mater. Process. Technol. 251, 146–159. https://doi.org/10.1016/j.jmatprotec.2017.08.021.